



HAL
open science

Micropipette Force Probe to quantify single-cell force generation: application to T cell activation

Anna Sawicka, Avin Babataheri, Stéphanie L Dogniaux, Abdul I. Barakat, David Gonzalez-Rodriguez, Claire L Hivroz, Julien Husson

► To cite this version:

Anna Sawicka, Avin Babataheri, Stéphanie L Dogniaux, Abdul I. Barakat, David Gonzalez-Rodriguez, et al.. Micropipette Force Probe to quantify single-cell force generation: application to T cell activation. *Molecular Biology of the Cell*, 2017, 28 (23), pp.3133-3470. 10.1091/mbc.E17-06-0385 . inserm-01613825

HAL Id: inserm-01613825

<https://inserm.hal.science/inserm-01613825v1>

Submitted on 10 Oct 2017

HAL is a multi-disciplinary open access archive for the deposit and dissemination of scientific research documents, whether they are published or not. The documents may come from teaching and research institutions in France or abroad, or from public or private research centers.

L'archive ouverte pluridisciplinaire **HAL**, est destinée au dépôt et à la diffusion de documents scientifiques de niveau recherche, publiés ou non, émanant des établissements d'enseignement et de recherche français ou étrangers, des laboratoires publics ou privés.

TITLE

Micropipette Force Probe to quantify single-cell force generation: application to T cell activation

AUTHORS

Anna Sawicka^{†,‡}, Avin Babataheri[†], Stéphanie Dogniaux[‡], Abdul I. Barakat[†], David Gonzalez-Rodriguez[§], Claire Hivroz^{†,*}, Julien Husson^{†,*}

*For correspondence: claire.hivroz@curie.fr (CH), julien.husson@ladhyx.polytechnique.fr (JH).

AFFILIATIONS

[†]Laboratoire d'Hydrodynamique (LadHyX), Department of Mechanics, Ecole polytechnique-CNRS UMR7646, 91128 Palaiseau, France.

[‡]Institut Curie Section Recherche, INSERM U932 & PSL Research University, Paris, France.

[§]LCP-A2MC, Institut Jean Barriol, Université de Lorraine, 1 bd Arago, 57078 Metz, France.

RUNNING HEAD

Micropipette Force Probe to quantify single-cell force generation

KEYWORDS

T lymphocytes, adaptive immunity, cell mechanics, force generation, CD4+ T cells, helper T cells

ABBREVIATIONS

MFP, Micropipette Force Probe; BFP, Biomembrane Force Probe; AFM, Atomic Force Microscopy; SEM, Scanning Electron Microscopy

ABSTRACT

In response to engagement of surface molecules, cells generate active forces that regulate many cellular processes. Developing tools that permit gathering mechanical and morphological information on these forces is of the utmost importance. Here we describe a new technique, the Micropipette Force Probe, that uses a micropipette as a flexible cantilever that can aspirate at its tip a bead that is coated with molecules of interest and is brought in contact with the cell. This technique simultaneously allows tracking the resulting changes in cell morphology and mechanics as well as measuring the forces generated by the cell. To illustrate the power of this technique, we applied it to the study of human primary T lymphocytes (T cells). It allowed the fine monitoring of pushing and pulling forces generated by T cells in response to various activating antibodies and bending stiffness of the micropipette. We further dissected the sequence of mechanical and morphological events occurring during T cell activation to model force generation and to reveal heterogeneity in the cell population studied. We also report the first measurement of the changes in Young's modulus of T cells during their activation, showing that T cells stiffen within the first minutes of the activation process.

INTRODUCTION

In a variety of biological functions such as adhesion (Liu *et al.*, 2015), migration (Sheetz, 1994; Plotnikov and Waterman, 2013), mechanotransduction (Ingber, 1997), probing of the mechanical environment (Schaefer and Hordijk, 2015) or communication between cells (Basu and Huse, 2017), receptor-ligand binding triggers cells to generate forces. Understanding the interplay between biochemical and mechanical signals requires methods capable of quantification of forces in different biochemical and cellular environments.

To measure and characterize forces generated by cells, several techniques have been applied. They can be distinguished mostly by the type of force probe they use. Atomic Force Microscopy (AFM) uses a flexible cantilever coated with molecules of interest to measure forces exerted by cells attached to a flat surface (Pelling *et al.*, 2007; Ossola *et al.*, 2015; Rigato *et al.*, 2017). In Traction Force Microscopy (Dembo and Wang, 1999; Hui *et al.*, 2015; Hui and Upadhyaya, 2017) flexible substrates with embedded fluorescent beads or flexible micropillars are deformed by the cells plated on them. DNA tension probes use a ligand immobilized to a surface through a DNA tether which is unfolded when a sufficient force is applied by the cell, leading to a change in fluorescence signal (Wang and Ha, 2013; Liu *et al.*, 2016). Lastly, the Biomembrane Force Probe (BFP) uses a red blood cell to which molecules of interest are bound via an attached coated bead (Simson *et al.*, 1998; Merkel *et al.*, 1999; Pincet and Husson, 2005; Heinrich and Ounkomol, 2007; Gourier *et al.*, 2008; Husson *et al.*, 2011; Sun *et al.*, 2011; Šmít *et al.*, 2017).

Micropipettes are most often used to probe by aspiration the passive mechanical properties of cells (Evans and Kukan, 1984; Sato *et al.*, 1987; Needham and Hochmuth, 1992; Shao and Hochmuth, 1996; Sit *et al.*, 1997; Hochmuth, 2000; Spillmann *et al.*, 2004; Hogan *et al.*, 2015) or their dynamical response upon controlled stimulation (Evans *et al.*, 1993; Herant *et al.*, 2005, 2006; Lee *et al.*, 2015). We herein describe the Micropipette Force Probe (MFP) that uses a flexible micropipette directly as the force probe. It allows spanning a large range of probe stiffness with micropipettes of different geometry. Holding the cell and its target allows dynamically following the morphological and mechanical properties of the triggered cells while measuring the forces generated. We illustrate the advantages of MFP by applying it to the study of T cell activation, following our previous studies in the field (Husson *et al.*, 2011; Guillou *et al.*, 2016b; Hivroz and Saitakis, 2016; Saitakis *et al.*, 2017) We provide new insights into this process of pivotal importance in the adaptive immune response.

RESULTS

Micropipette Force Probe

Concept / principle

The principle of the Micropipette Force Probe is to use a glass micropipette as a cantilever of known bending stiffness in order to measure forces generated by a single cell. The use of a micropipette instead of a filled microfiber or lamella (Meyhöfer and Howard, 1995; Tees *et al.*, 2001; Marcy *et al.*, 2004; Guillou *et al.*, 2016a) allows forming a force probe tailored to the particular experiment, with a bead covered with antibodies of interest aspirated at the tip of the micropipette (called the bead micropipette herein). Then, a cell held by a second, rigid micropipette (called the cell micropipette herein) is brought in contact with the bead, and the response of the cell to the bead is recorded. Of practical importance, once the response of the cell is finished, both bead and cell can be released from their respective micropipettes, and another bead and cell can be selected within a couple of minutes, in order to perform another experiment. The technique thus allows testing tens of different bead-cell couples with a single set of micropipettes, minimizing uncertainty due to micropipette variability. Moreover, the technique allows using virtually any kind of bead: commercially available or custom made with any chemical coupling (Husson *et al.*, 2011). Experiments are performed on an inverted microscope with two micropositioners holding and moving both micropipettes, the tips of which lie in the focal plane of the microscope where both cell and bead are observed (Figure 1A-B). During a standard experiment, the contact between a cell and the bead micropipette is ensured by compressing the cell against the bead (Figure 1B top, Video 1). The base of the bead micropipette remains immobile, so that any movement of the bead is due to the forces generated by the cell (pushing or pulling on the bead, Figure 1B bottom).

Range of application and limitations

The measured force is proportional to the bead micropipette's tip displacement in the microscopy image. To achieve a measurable displacement, the bending stiffness of the bead micropipette needs to be adapted to the range of forces exerted by the cell. With different shapes of bead micropipettes, a wide range of bending stiffness can be attained: from 0.01 nN/ μm to >100 nN/ μm . This range is wider than for existing force probes: optical tweezers have a typical stiffness in the 0.01-0.5 nN/ μm range, and AFM cantilevers are usually stiffer than 10 nN/ μm . In practice, when studying T cells as demonstrated in this paper, we used a typical bending stiffness ranging from 0.15 nN/ μm to 1.10 nN/ μm . Our detection accuracy is better than 0.05 μm , leading to a resolution in force from 0.008 to 0.06 nN depending on the bending stiffness of the bead micropipette. Here we apply the technique to non-adherent blood cells, but it can also be applied to adherent cells grown on a large bead substrate such as dextran beads, as already shown for endothelial cells (Guillou *et al.*, 2016a). The technique also allows monitoring cell morphology seen from profile during the force measurements.

We detect displacement of the bead micropipette by live analysis of camera images, with a limited time resolution (typically 400 Hz, see Methods) as opposed to superior time resolution of laser diodes used in AFM. The bead micropipettes have a several millimeter-long, flexible shaft subjected to several sources of vibrations. The softer the micropipette, the larger the vibrations amplitude. The major source of vibrations is a free medium-air interface in an open Petri dish in which the experiments are performed. These vibrations can be controlled with an experimental chamber made of glass slides holding a liquid droplet by capillarity (Pincet and Husson, 2005; Gourier *et al.*, 2008) (Supplemental Figure S1). Since the use of the chamber makes experiments

less easy to implement, we used open Petri dishes for all experiments reported in this paper. Vibrations can also come from vibrating devices such as the fan of the camera cooling system. Altogether, these vibrations limit the accuracy of force and displacement measurement. The bead micropipette, while firmly holding the bead, does not form a perfectly tight joint with it and can thus aspirate small pieces of cell membrane. Once such aspiration is clearly visible, we stop the measurements for this cell, although aspiration of micron-size parts of the cell membrane does not appear to affect the cell behaviour. These cell debris, however, might block the bead micropipette, precluding its further use.

Comparison with the Biomembrane Force Probe

We previously studied the mechanics of T cell activation using a Biomembrane Force Probe (BFP) (Husson *et al.*, 2011). This device uses a red blood cell as a spring of calibrated stiffness ranging from ~ 0.05 to ~ 0.5 nN/ μm (Simson *et al.*, 1998; Merkel *et al.*, 1999; Pincet and Husson, 2005; Heinrich and Ounkomol, 2007; Gourier *et al.*, 2008; Sun *et al.*, 2011; Šmit *et al.*, 2017). The range of stiffness is similar to the one used with the Micropipette Force Probe (MFP), but the measurements with the BFP are limited to pulling forces and to displacements smaller than ~ 0.3 μm . The MFP was designed to overcome these two important limitations of the BFP. With MFP we are able to measure pushing forces over larger displacements (more than 2 μm). On the practical side, we wanted to use any kind of bead size and coverage, and reuse the same probe (bead micropipette) with several cells in a row. We validated that results obtained with the MFP and BFP were consistent by measuring the pulling forces generated by human primary CD4+ T cells (Supplemental Figure S2).

Application to T cell activation

There is growing interest in the forces generated by T cells, because these forces are involved in formation of the immune synapse and T cell activation (reviewed in (Depoil and Dustin, 2014; Comrie and Burkhardt, 2016; Hivroz and Saitakis, 2016)). Using the BFP, we were among the first to show that human T cells exert forces when their T Cell Receptor (TCR) is engaged (Husson *et al.*, 2011).

To further study these forces, we applied the MFP technique to the events occurring during the first 5-10 minutes after TCR/CD3 triggering (the first events during T cell activation). We used human primary CD4+ T cells (called resting T cells herein, see Methods) and beads covered with anti-CD3 antibodies. An experiment with the MFP started by bringing the cell in contact with the bead, thus inducing a slight compression of the cell (compressive force up to 0.15 nN, see x_{contact} in Figure 2A). We defined the time origin as the instant when this compression was applied, and we measured other times described below relative to this initial contact time.

Pushing forces

The first measurable mechanical event during T cell activation was the appearance of a pushing protrusion that we call a punch. The punch pushed the bead away at a speed v_{push} that was constant to a first approximation (Figure 2A). The punch appeared, and the pushing force started, at instant $t_{\text{push}} = 31$ s (median, interquartile range (IQR): 22-42 s, N=112 cells across 14 experiments) with resting T cells and anti-CD3/anti-CD28 beads. This t_{push} was similar for resting T cells activated with beads covered with only anti-CD3 antibodies ($t_{\text{push}} = 24$ s median, IQR: 18-30 s, N=20 cells across 2 experiments). Upon reactivation of T cells the t_{push} was shorter, as shown for the CD4+ T lymphoblasts (called pre-activated herein) with anti-CD3/anti-CD28 beads ($t_{\text{push}} = 18$ s median, IQR: 12-33 s, N=19 cells across 2 experiments) (Figure 2C). The punch grew initially at an approximately right angle from the cell body (Video 1), which we confirmed by scanning electron

microscopy (Supplemental Figure S3A). No punch formed when we put resting T cells in contact with beads covered with anti-CD45 antibodies (Video 2), showing that the pushing force required TCR/CD3 engagement.

Tail retraction

The cell was partly aspirated in the cell micropipette due to an aspiration pressure of typically 80 Pa that was kept constant throughout the experiment. We called the part of the cell inside the micropipette the tail and measured its length, L_{tail} (Figure 1B). A shortening of the tail indicates an increase in cell tension, which is itself directly linked to the effective Young's modulus, or effective stiffness, of the cell that we can directly quantify using profile microindentation (Guillou *et al.*, 2016a, 2016b). During T cell activation, we observed a shortening of the tail (Figure 2B) beginning at instant $t_{tail}=38$ s (median, IQR: 27-61 s, N=103 cells across 14 experiments). The time at which the tail begins to retract is similar for resting CD4+ T cells activated with anti-CD3 beads. The measured t_{tail} is also similar for resting and pre-activated CD4+ T cells in contact with anti-CD3/anti-CD28 beads (Figure 2C). To directly quantify changes in cell tension related to these changes in tail length, we performed profile microindentations (Guillou *et al.*, 2016a) during the activation of resting T cells (Figure 1C). The effective Young's modulus of T cells increased from 128 ± 16 Pa to 292 ± 44 Pa (mean \pm s.e.m., timepoints $t=-10$ s and $t=70$ s, N=15 and 9 cells, respectively, across 2 experiments, Figure 2D). This increase began 30-40 s after the contact (Figure 2D), consistent with the measured time of retraction, t_{tail} . Although pushing and tail retraction began within a narrow time window (Figure 2C), for the majority of resting T cells activated with anti-CD3/anti-CD28 beads pushing preceded tail retraction ($t_{push} < t_{tail}$ for 76 cells, $t_{push} > t_{tail}$ for 26 cells, across 14 experiments).

Cell forces and speeds depend on bending stiffness of the bead micropipette

In a previous study we showed that T cells could adapt their pulling forces to the stiffness of the substrate against which they develop these forces (Husson *et al.*, 2011). The MFP allowed us to investigate the dependence of both pushing and pulling forces on the stiffness of the substrate. We found that for each cell the pushing speed, hence the loading rate $dF/dt = kv$, were relatively constant over time (Figure 2A) but depended on the bending stiffness of the bead micropipette (Figure 2E). We then wanted to measure the growth speed of the punch when no resisting force was applied (approximating $k=0$). We first attempted to do so by releasing the bead from the bead micropipette right after the contact was established. In this case a punch grew, but quickly either became very curved, or grew out of the focal plane, so we could not quantify its growth speed. We therefore used the approach shown in Figure 1D, in which a cell was brought in contact with the bead, and when the punch started growing from the cell, the cell micropipette was manually retracted to keep the bead micropipette at its initial position. This allowed us to observe the punch growing against no notable resisting force, which simulates a bead micropipette with a vanishing bending stiffness. Hence, we measured a data point that would correspond to $k=0$ in Figure 2E (red star). Consistent with the trend of growth speed diminishing with increasing bending stiffness k , this growing speed at $k=0$ was the largest.

Buckling and end of punch growth

After 10 s (median, IQR: 8-18 s, N=79 cells across 14 experiments) of pushing at a constant speed, the punch suddenly stopped growing and stalled for 2 s (median, IQR: 1-4 s, N=36 cells across 6 experiments), as it can be seen on the $x_{bead}(t)$ chart (inset on top in Figure 3A). The punch then usually resumed its growth but in another direction and with a broader shape (Video 1, Supplemental Figure S4). In most of the cases this stalling corresponded to a kink appearing close to the middle of the punch (arrow in Video 1). We called this event buckling. The force measured at

this moment, $F_{buckling}$, in the range of 0.15 to 0.30 nN, depended on the bending stiffness of the bead micropipette, k (Figure 3B). The mathematical shape of this dependence was consistent with the theory of mechanical buckling: the critical force $F_{buckling}$ to induce buckling of an elastic beam of elastic modulus E , moment of inertia I , and length L is given by Euler's formula:

$$F_{buckling} = \frac{\pi^2 EI}{L^2}. \quad (1)$$

The compressive force exerted on the punch by the probe is $F = kL$, where k is the bending stiffness of the bead micropipette. Therefore, the expected dependence of the buckling force on bending stiffness of the bead micropipette is

$$F_{buckling} = k^{2/3} (\pi^2 EI)^{1/3} \quad (2)$$

Figure 3B shows a comparison between force predicted by Equation (2) and the $F_{buckling}$ measured for different values of bending stiffness of the bead micropipette. To yield the predictions shown in Figure 3B, Equation (2) was applied for $E = 130$ Pa (mean value measured by profile microindentations, see above in Tail retraction), the punch was assumed to be a cylinder with a moment of inertia $I = \pi D^4/64$, and the punch diameter D was adjusted to fit the experimental data, leading to $D=1.3$ μm , slightly smaller than the measured final diameter of 1.9 μm (see below). The fact that Euler's formula correctly described the observed dependence between force and bending stiffness of the bead micropipette supported our hypothesis that the observed warping of the punch corresponds to mechanical buckling.

After buckling, the punch usually resumed its growth, with similar pushing speed (0.086 ± 0.025 $\mu\text{m/s}$ vs 0.098 ± 0.029 $\mu\text{m/s}$, mean \pm s.d., $N=21$ cells across 5 experiments, $p=0.05$, two-tailed paired t-test, see Supplemental Figure S5) but a different morphology. For larger bending stiffness of the bead micropipette (above 0.35 nN/ μm) the punch did not regrow after buckling, it buckled only at its maximal length. On average, the punch reached a maximal length of 2.0 ± 0.7 μm (mean \pm s.d., $N=106$ cells across 14 experiments) with a diameter of 1.9 ± 0.5 μm (mean \pm s.d., $N=105$ cells across 14 experiments, Figure 3D), i.e. roughly half the diameter of the 4.5 μm -wide bead. At this point the cell generated a maximal pushing force, F_{push}^{max} , up to 0.8 nN. This force also depended on the bending stiffness of the bead micropipette (Figure 3B). The maximal pushing forces were similar in amplitude when resting T cells were activated with anti-CD3/anti-CD28 beads and with anti-CD3 beads. Pushing forces were also similar for resting and pre-activated CD4+ T cells activated with anti-CD3/anti-CD28 beads (Figure 3B). Treatment with ML-7, the Myosin Light Chain Kinase inhibitor, led to longer punches (Figure 3B, ML-7: 2.35 ± 0.12 μm , $N=17$ cells across 3 experiments, control: 1.97 ± 0.07 μm , $N=106$ cells across 14 experiments), but to the same maximal pushing force (Figure 3D, see below for further observations with ML-7).

Collapse of the punch and formation of a cup

Once the punch had reached its maximal length, it gradually became broader while collapsing at a constant speed, v_{return} (Figure 3A) and then formed a cup-like structure on the bead (called a cup herein, Video 1). Some cells did not form the cup but kept on pushing instead, growing and collapsing several punches in a row. These cells did not reach the further stages described below. During the collapse of the punch, the bead moved backwards to its initial position (Figure 3A). Even though the punch underwent a large morphological change, for a given cell and bending stiffness of the bead micropipette, the return speed and pushing speed had the same absolute value (Figure 3A inset at bottom). Interestingly, ML-7 treatment did not change the pushing speed (Figure 3C showing pushing and pulling loading rate). However, it reduced both the return speed (ML-7: $v_{return}=0.044 \pm 0.006$ $\mu\text{m/s}$, $N=21$ cells across 3 experiments, at $k=0.208$ nN/ μm as averaged over $k=0.189$ to 0.218 nN/ μm , control: $v_{return}=0.085 \pm 0.009$ $\mu\text{m/s}$, mean \pm s.e.m., $N=25$ cells across 4 experiments, at $k=0.195$ nN/ μm as averaged over $k=0.146$ to 0.202 nN/ μm) and the pulling speed (ML-7: $v_{pull}=0.021 \pm 0.004$ $\mu\text{m/s}$, $N=10$ cells across 3 experiments, control: $v_{pull}=0.042 \pm 0.006$ $\mu\text{m/s}$,

mean \pm s.e.m., N=11 cells across 3 experiments).

The cup contacted the bead with a larger area than the punch. The cup reached a covering angle $\alpha=121\pm 21^\circ$ (mean \pm s.d., N=27 cells across 6 experiments, cup angle α defined in Figure 3A), with the rim of the cup sometimes reaching the tip of the bead micropipette (Video 1). To check if this perturbed the normal spreading of the cup, we used a different bead micropipette shape, with a 90° bend at the tip. This way the bead was aspirated at the intersection with the x-axis, further away from the cell than in the standard situation, leaving more space for eventual cup spreading (Supplemental Figure S6). In this configuration, the measured cup angle was $140\pm 17^\circ$ (mean \pm s.d., N=30 cells across 4 experiments) showing that the cell spreading on the bead was not strongly perturbed by the tip of the bead micropipette. Pre-activated T cells visibly spread more on the bead (Video 3) than resting T cells; in that case the measured cup angle reached $179\pm 58^\circ$ (mean \pm s.d. N=18 cells across 2 experiments, Figure 3D).

Lag phase

After the punch collapsed and the cup formed as described above, the cell entered what we called a lag phase. During this phase the cell exerted no large forces on the bead, which stayed close to its initial position ($x_{bead}=0$). However, the cell remained active as shown by its morphology: waves and/or ruffles formed on the cell surface and travelled seemingly from the cup towards the tail (Video 1). The lag phase lasted for 51 s (median, IQR: 16-76 s, N=56 cells across 14 experiments, measured as $\Delta t_{lag}=t_{pull} - t_{lag}$, Figure 3A) and ended with the onset of a pulling force exerted by the cell on the bead at $t_{pull}=148$ s (median, IQR: 104-226 s, N=63 cells across 14 experiments).

Pulling phase

As when T cells pushed, they pulled the bead at a relatively constant speed, v_{pull} , or a constant loading rate $dF/dt = kv_{pull}$, that depended on the bending stiffness of the bead micropipette k . For the same bending stiffness of the bead micropipette, the pulling loading rate was roughly twice smaller in absolute value than the pushing loading rate (Figure 3C). Maximal pulling forces reached 0.8 nN in magnitude (Figure 3C inset), comparable to maximal pushing force.

We investigated whether the pulling phase dynamics could be described by a recent model by Etienne et al. (Étienne *et al.*, 2015), which was developed to characterize contractile forces of different cell types (rat embryonic fibroblasts and the mouse myogenic cell line) adhering to two opposite glass lamella. Etienne et al. proposed a minimal model, accounting for cell viscoelasticity, actomyosin contractility and actin treadmilling, to explain the dependence of pulling forces on the stiffness of the substrate against which cells develop forces. In this model, at the early times of pulling, when the pulling force is significantly below its maximum, the rate of force increase over time is described by

$$\frac{dF}{dt} = \begin{cases} k v_c & \text{if } k < k_{crit}, \\ \frac{\sigma_a S}{\tau_\alpha} & \text{otherwise.} \end{cases} \quad (3)$$

Here, k is the stiffness of the substrate, v_c is the typical actomyosin contractile velocity, σ_a is the maximum active contractile tension that can be developed, S is the cross-section of the cup (contact area between the cell and the substrate), and τ_α is the typical time for actomyosin stress relaxation. According to Eq. (3), the pulling loading rate dF/dt increases linearly with the stiffness of the substrate k , provided that k remains small compared to the cell stiffness, $k_{crit} = ES/L_0$, where E is the Young's modulus and L_0 is the maximal probe deformation allowed by the geometry of the experiment. Beyond $k=k_{crit}$, the probe would be more rigid than the cell, and the rate of pulling would become independent of the probe and limited by the rate of actomyosin relaxation. We applied the model to our experimental data on the dependence of dF/dt on k during the pulling

phase, shown in Figure 3C. As predicted by the model, experiments in the range of bending stiffness of the bead micropipette studied here were satisfactorily described by a proportionality relation, represented by a straight line of slope $v_c = 0.017 \mu\text{m/s}$ (95% c.i. $0.013 \div 0.020 \mu\text{m/s}$). This value is consistent with the $v_c = 0.025 \mu\text{m/s}$ deduced by Etienne et al. (Étienne *et al.*, 2015) for experiments on mouse myoblasts. For myoblasts, Etienne et al. observed a second regime, corresponding to a constant rate of pulling force generation, in experiments with very stiff probes of $k > k_{\text{crit}} \approx 10 \text{ nN}/\mu\text{m}$, which is beyond the range of bending stiffness explored here. The fact that this second regime was not attained in our experiments using bending stiffness of the bead micropipette up to $1 \text{ nN}/\mu\text{m}$ implies that the final Young's modulus of the mature T cell's cup is larger than 1 kPa . Overall, the ability of Etienne et al.'s model to describe our experimental results suggests that T cell force generation during the pulling phase arises from biophysical mechanisms shared by other cell types.

Identification of two different cell morphologies after pulling

At the end of the pulling phase, at $t_{\text{end}}=202 \text{ s}$ (median, IQR: 136-290 s, N=49 cells across 8 experiments), we observed two different T cell morphologies (Figure 4, Video 4). We called the first morphological type nepenthes, after the shape of the nepenthes flower, and the second one flytrap, by analogy, as it seemingly closed on the bead and rounded up around it. The flytrap cells usually extracted themselves from the cell micropipette within 5 minutes from contact (Video 4). The nepenthes cells usually stayed in their micropipette, remained elongated and showed extensive activity in the form of waves travelling along the cell body. Some flytrap cells showed some waves but not as clearly and over a shorter period of time than nepenthes cells. The tail of nepenthes cells regrew in the cell micropipette for 40% of nepenthes cells (12 out of 30 nepenthes cells across 8 experiments) and never for flytrap cells (23 flytrap cells across 8 experiments). Nepenthes cells had a clear uropod morphology at the opposite side to the bead (Video 5), whereas flytrap cells did not have any clear uropod. This different morphology could be clearly seen with SiR-actin, a fluorescent dye binding F-actin: it showed a crescent shape structure for flytrap cells and a point-like uropod for nepenthes cells (Supplemental Figure S7, Video 6). With anti-CD3 beads we observed both types (6 nepenthes cells, 9 flytrap cells, across 22 cells in 2 experiments). Pre-activated T cells showed a clear tendency towards the flytrap type (20 cells, all flytrap cells in 2 experiments).

The assignment of a cell to the flytrap or nepenthes type was not possible in about 30% of cells in micropipette experiments (24 out of 77 resting T cells activated with anti-CD3/anti-CD28 beads in 8 experiments, 7 out of 22 resting T cells activated with anti-CD3 beads in 2 experiments), usually when the cell was not well aligned with the bead at the contact or pushed itself out of the focal plane during the activation process. Images with no micropipettes (Videos 5-6, Scanning Electron Microscopy images in Figure 4) showed that both phenotypes were not an artefact due to the micropipette setup. These two archetypal morphologies reveal a heterogeneity of behavior of resting CD4+ T cells in the very early stages of activation.

DISCUSSION

MFP as a new technique for the measurement of forces generated by cells

Several micromanipulation techniques have been developed to measure forces actively generated by cells. Some are limited by the range of forces they can measure (e.g. optical tweezers, for forces lower than $\sim 100 \text{ pN}$) and are thus best suited for single-molecule measurements, or specific studies such as forces generated by single filopodia (Bornschiogl *et al.*, 2013). Single cells generate active forces ranging from tens of piconewtons to several nanonewtons. Relevant techniques to measure these forces rely mainly on the tracking of the deflection of a calibrated

spring: AFM cantilevers (Binnig *et al.*, 1986; Puech, 2005), microfibers or glass lamella (Howard and Hudspeth, 1987; Ishijima *et al.*, 1996; Tees *et al.*, 2001; Marcy *et al.*, 2004; Desprat *et al.*, 2006; Tsukasaki *et al.*, 2007; Mitrossilis *et al.*, 2010), or flexible substrates or micropillars (Dembo and Wang, 1999; Hui *et al.*, 2015; Hui and Upadhyaya, 2017).

While micropipettes were often used to aspirate cells in order to probe their passive mechanical properties (Evans and Kukan, 1984; Sato *et al.*, 1987; Needham and Hochmuth, 1992; Shao and Hochmuth, 1996; Sit *et al.*, 1997; Hochmuth, 2000; Spillmann *et al.*, 2004; Hogan *et al.*, 2015) or their dynamical response upon controlled stimulation (Evans *et al.*, 1993; Herant *et al.*, 2005, 2006; Lee *et al.*, 2015), they were seldom used as flexible cantilevers, as it was done for instance to measure adhesion (Colbert *et al.*, 2009). The micropipette force probe (MFP) described here uses the micropipette as a flexible cantilever to measure forces generated by single cells. This study highlights the possibilities brought up by MFP. Thanks to the observation of the morphology of the cells during the force measurement, we describe in detail the various phases of force generation during T cell activation. For instance, we identified the pushing protrusion, punch, thanks to the bead micropipette which held the punch along a fixed axis during its growth. Without this support punch rapidly bent and was barely noticeable (Video 5). Importantly, the simultaneous observation of cell morphology allows fine control of the cell-bead contact time, which is not possible when injecting beads and cells in a Petri dish. A modified version of AFM (lateral AFM (Ounkomol *et al.*, 2009)), allows sideways imaging while measuring forces, but the experiments with cells require replacing the AFM cantilever for every cell. This arguably becomes easier with MFP, as the bead micropipette can be reused multiple times.

The application of MFP to the study of T cell activation led to measurements consistent with previous studies. Our measurements of human T cells performed at the whole-cell (and nanonewton) level are highly complementary to recent measurements by Liu *et al.* using DNA tension probes (Liu *et al.*, 2016), who showed that around 40 s after mouse OT-1 resting T cells came into contact with the activating surface, piconewton pulling forces were generated at the TCR. A more direct comparison to our MFP measurements is provided by the results of Hu and Butte (Hu and Butte, 2016), who performed AFM measurements on mouse OT-1 pre-activated T cells (lymphoblasts). They measured similar pushing forces (0.1-1.2 nN) and somewhat larger (0.5-2.5 nN) pulling forces. This suggests that forces of the described magnitude and timing form integral part of the process of T cell activation.

New information on T cell activation obtained with MFP

MFP was particularly useful for identifying and measuring the pushing forces developed by human T cells upon TCR/CD3 triggering. Like pulling forces, pushing forces were sensitive to bending stiffness of the bead micropipette. The maximal measured pushing force was approximately 0.4 nN, comparable to the force required to deform the glycocalyx, whose reported Young's modulus is 400 to 700 Pa (Bai and Wang, 2012; Marsh and Waugh, 2013). Thus, the pushing forces could serve to compress the glycocalyx covering the antigen-presenting cell (APC) and to form a stable contact between the T cell and the APC. On the molecular level, the pushing forces are also probably needed to „push away“ the bulky phosphatase CD45 that needs to be excluded from the TCR microclusters to allow signaling in T cells (Varma *et al.*, 2006).

The model we propose to understand the observed buckling of the growing punch is compatible with the structure of the punch we described earlier (Husson *et al.*, 2011), a hollow tube of polymerized actin. Together with the reported minor role of myosin activity (see results obtained with ML-7), the observed buckling behavior may provide insight into the molecular mechanisms involved in the formation of this structure. The punch is also probably involved in the ability of T cells to „palpate“ their environment and in particular, as shown herein, to sense its stiffness. This stiffness sensing is important since it leads to functional programming of the T cells (Saitakis *et al.*, 2017). The development of forces perpendicular to the contact area is probably also important for T cells to cross the endothelial barrier by the path of least resistance (Martinelli *et al.*, 2014).

Our results also show that the presence of the activating CD28 antibody together with the

activating TCR/CD3 antibody altered the pushing forces developed by the resting T cells by modifying the length and diameter of the growing punch. These data add to the reported effect of the engagement of CD28, which has been shown by traction force microscopy to increase the traction forces developed by human primary T cells activated by TCR/CD3 (Bashour *et al.*, 2014). This is in agreement with the known effect of CD28 on actin remodeling (Wülfing, 1998). It would thus be particularly interesting to investigate the role of WAVE2 and cofilin, two regulators of CD28-induced actin dynamics (Roybal *et al.*, 2016) on the pushing forces reported herein.

The MFP experimental setup also allowed us to compare primary, resting and pre-activated, effector T cells in terms of their ability to develop forces. Our results reveal that pre-activated T cells, when their CD3 and CD28 receptors were triggered again, developed pushing forces earlier and grew a longer and broader punch (Figures 2C, 3D). This probably enables them to better probe their environment. Since forces were linked to the killing efficiency of mouse cytotoxic T cells (Basu *et al.*, 2016), this may also explain the better efficiency of effector T cells in killing their targets.

Finally, as the experiments with MFP are conducted in open Petri dishes, the technique is versatile and complementary experiments can be implemented, such as profile microindentation during activation (with a third micropipette added, Figure 1C). This way we were able to measure the Young's modulus of T cells during their activation and to show that they got stiffer when activated (Figure 2D). This change in the mechanical properties means that the actomyosin cytoskeleton undergoes drastic modifications during T cell activation. As a result, an extremely soft T cell (80 to 100 Pa, (Bufi *et al.*, 2015; Guillou *et al.*, 2016b) becomes more rigid, which may well be sensed by the antigen presenting cell (APC) and participate in the cross-talk between the T cell and the APC.

We applied the MFP technique to investigate the role of myosin in the development of both pushing and pulling forces by T cells. Our results show that pushing speeds (and hence pushing loading rates) remain unchanged for resting T cells treated with the myosin light chain kinase inhibitor ML-7 (Figure 3C). These data are in agreement with results obtained with AFM showing a relatively low effect of ML-7 on the pushing forces (Hu and Butte, 2016). They suggest that the pushing forces are essentially due to the actin polymerization. This is in agreement with reports showing that inhibition of the phosphorylation of the myosin light chain with the Rho kinase inhibitor Y-27632 or inhibition of the myosin II ATPase activity with blebbistatin does not alter actin retrograde flow at the immune synapse (Babich *et al.*, 2012; Ashdown *et al.*, 2017). In contrast, ML-7 treatment affects the punch length, which is longer (Figure 3D), and both the return and the pulling speeds, which are reduced, suggesting that myosin activity controls the shrinkage of the punch and the subsequent generation of pulling forces. These data are consistent with results obtained by traction force microscopy on Jurkat cells (Hui *et al.*, 2015; Hui and Upadhyaya, 2017) and by AFM on pre-activated mouse T cells (Hu and Butte, 2016), which both show that pulling forces developed by T cells are affected by pharmacological inhibitors of myosin.

In the present study we identified and characterized two different morphologies adopted by T cells during their activation. The difference in nepenthes versus flytrap formation did not correlate with the naive versus memory phenotype of the T cells (data not shown). However, this difference of behavior may well be due to the presence of different T cell subpopulations in the purified CD4+ T cells used herein. Alternatively, the different phenotypes may also correlate with the difference between kinapse and synapse formation (Dustin, 2008). Indeed, waves of actin have been associated with a migratory phenotype (Inagaki and Katsuno, 2017), whereas phagocytic synapse (flytrap morphology) requires T cell arrest (Niedergang *et al.*, 2016). It would also be interesting to investigate if these two archetypal phenotypes lead to different functional outcomes.

Our results show that the MFP is particularly well suited to the analysis of pushing and pulling forces that cells generate in response to various triggering signals and various stiffness of the substrate they contact. It can also be coupled to profile microindentation to provide in real time the measurement of changes in mechanical properties of cells and gather many dynamic

morphological parameters. Together, these parameters reveal heterogeneity in the studied cell population and can be used to develop models explaining the forces generated at the cellular level in response to a given stimulus.

MATERIALS AND METHODS

Micropipette pulling and calibration

Micropipettes used to hold the cells (cell micropipettes) were prepared as described previously (Guillou *et al.*, 2016a): borosilicate glass capillaries (1 mm OD, 0.78 mm ID, Harvard Apparatus, Holliston, MA, USA) were pulled with a P-97 micropipette puller (Sutter Instruments, Novato, CA, USA). An MF-200 microforge (World Precision Instruments (WPI), Sarasota, FL, USA) was used to cut the tip of pulled capillaries to the desired inner diameter (2.5-3.5 μm). The diameter was first assessed optically with calibrated graduations in the microforge's ocular and then measured under the inverted microscope with the 100 \times objective. The micropipettes were then bent at a 45 $^\circ$ angle with an MF-900 microforge (Narishige, Tokyo, Japan) so that their tip was in the microscope's focal plane (Figure 1A).

Flexible micropipettes used to hold the beads (bead micropipettes) were pulled with a thin tip whose geometry determines the bending stiffness of the bead micropipette, k . We first cut the tip of the micropipette to the desired length with a melted glass bead on the MF-200 microforge. We then either bent the tip at right angle for the face-to-face cell-bead presentation (Supplemental Figure S6), or left it straight, as used in most of the experiments (Figure 1). Lastly, we bent the micropipette at a 45 $^\circ$ angle with the MF-900 microforge, to place the tip in the focal plane, as with the cell micropipette.

Microindenters were prepared from the bead micropipettes, as described previously (Guillou *et al.*, 2016a, 2016b) (see video in reference (Guillou *et al.*, 2016b)). In brief, the MF-200 microforge was used to melt glass at the tip of the micropipette, producing a glass bead of 5 to 10 μm in diameter. The diameter was then precisely determined under the microscope with the 100 \times objective.

The bending stiffness of microindenters and bead micropipettes was measured against standard microindenters that had been previously calibrated (Supplemental Figure S8). The standard microindenters were calibrated with a commercial force probe (model 406A with a force range of 0-500 nN, Aurora Scientific, Aurora, ON, Canada). The microindenters used in this paper had typically the rigidity of 0.5 nN/ μm , and the bead micropipettes in the range of 0.15-1.10 nN/ μm .

Beads and inhibitors

Dynabeads Human T-activator CD3/CD28, Dynabeads CD3, and Dynabeads CD45 (referred to as anti-CD3/anti-CD28, anti-CD3, and anti-CD45 beads, respectively) were purchased from Invitrogen Life Technologies (Carlsbad, CA, USA). ML-7 was purchased from Merck Millipore (Billerica, MA, USA), and suspended in DMSO (Pan-Biotech, Aidenbach, Germany). Cells were pre-incubated with 30 μM ML-7 for 15 minutes, and kept in the same concentration of the inhibitor throughout the experiment.

Cell purification and culture

All cells used in this study were human cells. This study was conducted according to the Helsinki Declaration, with informed consent obtained from the blood donors, as requested by the Etablissement Français du Sang. The complete medium was RPMI 1640 with GlutaMax, supplemented with 10% heat-inactivated Fetal Bovine Serum (FBS) and 1% penicillin-streptomycin (all from Gibco ThermoFisher Scientific, Waltham, MA, USA). Human primary CD4 $^+$ T cells were negatively selected from PBMCs isolated from the blood of healthy donors with the CD4 $^+$ T cell

isolation kit (Miltenyi Biotec, Bergisch Gladbach, Germany). Isolated T cells were suspended in FBS:DMSO (90%:10% vol/vol) and kept frozen in liquid nitrogen. 1-7 days before the experiment the cells were thawed, mixed with pre-heated complete medium, washed once, and then kept in the complete medium at 37°C, 5% CO₂, at a concentration of approximately 10⁶ cells/ml.

To obtain CD4⁺ T lymphoblasts, 6-well plastic plates were coated with anti-CD3 antibody (OKT3 clone, # 16-0037-85, eBioscience, ThermoFisher Scientific, 2.5 µg/ml in 1.3 ml final) overnight at 4°C. Wells were washed and 5.4x10⁶ freshly purified human primary CD4⁺ T cells were plated per well in the presence of soluble anti-CD28 antibody (LEAF Purified anti-human CD28 # BLE302923, Biolegend, San Diego, CA, USA, 2.5 µg/ml) and recombinant IL-2 (Proleukin, Novartis, Basel, Switzerland, 20 U/ml). Fresh medium containing IL-2 (20 U/ml) was added every 3 days and lymphoblasts were used from day 6, or frozen on day 6 and thawed before the experiment, as described above.

Western blot analysis of phosphorylation of the Myosin light chain

Human primary CD4⁺ T cells (4 × 10⁶/ml) were preincubated 15 min at 37°C with 30 µM ML-7 or in DMSO (vehicle 1/67, vol/vol). Cells were then activated by addition of anti-CD3/anti-CD28 beads at a ratio of one bead per cell. After described time (10 or 30 minutes), activation was stopped on ice by addition of cold PBS. After centrifugation, cells were lysed in Pierce RIPA buffer (ThermoFisher Scientific) supplemented with 1× complete, Mini, EDTA-free Protease Inhibitor Cocktail Tablet (Roche, Basel, Switzerland) and Halt Phosphatase Inhibitor Cocktail (ThermoFisher Scientific). Post-nuclear lysates were resolved by SDS-PAGE on Mini-PROTEAN TGX Precast Gels (Bio-Rad, Hercules, CA, USA) and were transferred to membranes (Immunoblot PVDF membranes, Bio-Rad) with the Trans-Blot turbo system (Bio-Rad). Membranes were blocked for 2 h in TBS, 5% BSA, 0.05% Tween and incubated overnight at 4°C with primary antibodies diluted in TBS, 5% BSA, 0.05% Tween: anti-Phospho-Myosin Light Chain 2 (Thr18/Ser19) rabbit Antibody (#3674, Cell Signaling Technology, Danvers, MA, USA, 1/1000) and anti-gp96 rat antibody (9G10 monoclonal rat antibody, Abcam, Cambridge, UK, 0.5 µg/ml). After several washes in TBS, 0.05% Tween, membranes were incubated 1 h at room temperature with HRP-conjugated secondary antibodies (Jackson ImmunoResearch, West Grove, PA, USA, 1/10 000) diluted in TBS, 5% BSA, 0.05% Tween. Membranes were then washed again, incubated for 5 min in Clarity Western ECL Blotting Substrates (Bio-Rad) and revealed with the ChemiDoc Touch Imaging system (Bio-Rad). Membranes are shown in Supplemental Figure S9.

Optical Microscopy

A glass-bottom Petri dish (Fluorodish, WPI) containing cells and activating beads was mounted on an inverted microscope (Nikon Eclipse Ti-U, Nikon Instruments, Tokyo, Japan) placed on an air table (Newport, Irvine, CA, USA). The microscope was equipped with a 100× oil immersion, 1.3 NA objective (Nikon) for monitoring the experiments and lower magnification objectives (40×, 20×, 10×, and 4×, Nikon) for micropipette positioning. Images were acquired with an ORCA-Flash 4.0 CMOS camera (Hamamatsu Photonics, Hamamatsu City, Japan) controlled with the MicroManager software (Edelstein *et al.*, 2014). The micropipettes were attached to two motorized micropositioners (Sensapex, Oulu, Finland). Beads were aspirated into the tip of the calibrated micropipette by capillarity forces with no aspiration pressure added. Cells were aspirated with 60-100 Pa of hydrostatic pressure applied with a water reservoir placed on a vertical linear slider (A1512DM-S1.5, Velmex, Bloomfield, NY, USA). The experiments were conducted close to 37°C; the dish was heated with heating pads (RS Components, Corby, UK) attached to the microscope table and an objective heating ring (Okolab, Pozzuoli, NA, Italy). No CO₂ buffering was used, instead, we replaced every hour during the experiment the medium in the dish. Time-lapse recordings were started just before the cell was gently brought into contact with the bead.

Micropositioning and detection

The bead was pushed or pulled by the cell along the X axis. The position of the bead, x_{bead} , is the same as the position of the tip of the bead micropipette. To track it, we developed a custom Matlab (Mathworks, Natick, MA, USA) code calling the Micromanager software. The gray levels along a line parallel to the X axis intersecting the micropipette were retrieved at acquisition frequency of about 300-500 Hz (depending on the size of the acquisition window). The gray levels along this line were cross-correlated with the gray levels of a template line acquired at the beginning of each recording (a strategy already used by the authors (Laan *et al.*, 2008; Husson *et al.*, 2009)). The position of the maximum of the cross-correlation function was locally fitted to a parabola and led to subpixellic precision of bead micropipette localisation (one camera pixel represents 64 nm with the 100x objective). In addition, a whole image was saved every 2 s, for the visualisation of the activation process.

Profile microindentation

Profile microindentation was performed as described previously (Guillou *et al.*, 2016a). Briefly, the setup consisted of a cell micropipette, a microindenter (see above in Micropipette pulling), and a rigid bead micropipette coming at a right angle (Figure 1C). Microindentation algorithm used the same method as in (Guillou *et al.*, 2016a) except that the software part was now implemented in Matlab in order to control directly the MicroManager software and obtain a higher acquisition frequency.

Scanning Electron Microscopy

For scanning electron microscopy the primary CD4+ T cells (1.5×10^5 cells per slide) were plated on slides pre-coated with 0.02% poly-L-lysine and incubated for 20 min at room temperature. Then, the anti-CD3/anti-CD28 beads were added, at a ratio of one bead per cell, and incubated for 5 min at room temperature. The samples were then washed in phosphate buffer pH 7.4 (PB), fixed overnight at 4°C in PB + 2% glutaraldehyde, and finally washed in PB. Samples were then dehydrated by passing through a graded series of ethanol solutions, then dried by the CO₂ critical-point method (CPD75 Quorum Technologies, Lewes, UK) and coated by sputtering with a 20-40 nm thin gold layer with a Scancoat Six (Edwards Vacuum, HHV, Crawley, UK). Acquisitions were performed with a GeminiSEM 500 microscope (Zeiss, Oberkochen, Germany).

Data analysis

From all the cells recorded in the micropipette experiments we excluded non-responding cells, which did not show any activity after the contact with the bead, and cells dead during recording, which retract the tail very fast, visibly grow larger in diameter and show no activity afterwards, presumably because they lose membrane integrity. Across all the experiments with anti-CD3/ anti-CD28 and anti-CD3 beads we recorded 486 cells from 10 different donors, out of which 84 cells were non-responding, 26 cells were dead during recording, and 376, or 77% of all cells, were active and were analyzed.

Morphological parameters of cells during activation (the diameter and the length of the punch, cup angle) were measured manually in the microscopy images, with the ImageJ software (Schneider *et al.*, 2012). For all experiments the contact time, used as instant $t=0$, was established in the image sequence. The onset of pushing and the onset of tail retraction were also marked in the images, and were used to calculate the t_{push} and t_{tail} (Figure 2A, 2C). The onset of pulling was established in the chart $x_{bead}(t)$ (as it is not associated with an abrupt change in cell morphology), and was used to determine t_{pull} . The lag time Δt_{lag} was calculated as the t_{pull} minus t_{lag} , which was also marked in the chart as the instant when $x_{bead}=0$ (Figure 3A). For force experiments, on the resulting $x_{bead}(t)$ charts we manually chose the beginning and the end of the pushing, return, and

pulling phases, and fitted a line for every slope. As the early experiments were performed with low sampling frequency (x_{bead} noted only once every 2 s, in the full image), the high sampling frequency data was appropriately averaged to consistently fit the v_{push} and v_{return} for all experiments which are shown in Figures 2E and 3B-C. Maximal pushing and pulling force was taken from the $x_{bead}(t)$ chart, as shown in the Figure 3A. Buckling force was also taken from the chart, the step in the pushing slope was verified with the corresponding frame in the image sequence, to check if it shows the described buckling morphology.

The profile microindentation experiments were analyzed as described previously (Guillou *et al.*, 2016a). Briefly, force vs indentation curves were fitted with the Hertz model to obtain the effective Young's modulus of the cell, assuming the Poisson's ratio equal 0.5. As the indentations continued during activation of the T cells, we discarded some experimental curves, for example when the bead interfered with the moving microindenter, or when the cell escaped from the cell micropipette.

Statistics

We report median times for all the events because the distribution is usually skewed with a few outliers with a very long time (see timeline in Figure 4). In the boxplots boxes span from the 1st to the 3rd quartile, with median marked with a thicker line. In the timing scatter plot (Figure 2D) we did not show (for resting T cells + anti-CD3/anti-CD28 beads) 1 t_{push} and 2 t_{tail} values larger than 200 s, for clarity of the chart; in the plot in Figure 4 we also did not show 5 data points at times >400s. All these values were included in the median and IQR calculations shown in the text. Mann Whitney test was used for comparing data in figures 2C. Unpaired t test with Welch's correction was used for comparing data in figures 3C.

ACKNOWLEDGMENTS

The authors thank Virginie Bazin (IBPS, Université Pierre et Marie Curie, Paris) for her help in obtaining SEM images. The authors acknowledge Caroline Frot, Antoine Garcia, Daniel Guy, Delphine L'Huillier, Sandrine Laguerre, Thérèse Lescuyer, Magali Tutou, and Do Chi Toai Vu, at LadHyX for technical support. The authors also thank Morgan Huse and Audrey Le Floc'h for fruitful discussions, and Pierre-Henri Puech for critical reading of the manuscript. This work has benefited from the financial support of the LabeX LaSIPS (ANR-10-LABX-0040-LaSIPS) managed by the French National Research Agency under the "Investissements d'avenir" program (n°ANR-11-IDEX-0003-02). This work was also supported by a GEFLUC Paris- Ile-de-France funding, a CNRS PEPS funding, an endowment in cardiovascular cellular engineering from the AXA Research Fund, funds from the DC-Biolabex (ANR-10-IDEX-0001-02 PSL* and ANR-11-LABX-0043) and from the Fondation pour la Recherche Médicale (FRM, FRM DEQ20140329513). AS is supported by a PhD fellowship from ITMO Cancer and the funds from the PhD Program Frontières du Vivant (FdV) – Cursus Bettencourt.

References

- Ashdown, G. W., Burn, G. L., Williamson, D. J., Pandžić, E., Peters, R., Holden, M., Ewers, H., Shao, L., Wiseman, P. W., and Owen, D. M. (2017). Live-Cell Super-resolution Reveals F-Actin and Plasma Membrane Dynamics at the T Cell Synapse. *Biophys. J.* *112*, 1703–1713.
- Babich, A., Li, S., O'Connor, R. S., Milone, M. C., Freedman, B. D., and Burkhardt, J. K. (2012). F-actin polymerization and retrograde flow drive sustained PLC β 1 signaling during T cell activation. *J. Cell Biol.* *197*, 775–787.
- Bai, K., and Wang, W. (2012). Spatio-temporal development of the endothelial glycocalyx layer and its mechanical property in vitro. *J. R. Soc. Interface* *9*, 2290–2298.
- Bashour, K. T., Gondarenko, A., Chen, H., Shen, K., Liu, X., Huse, M., Hone, J. C., and Kam, L. C. (2014). CD28 and CD3 have complementary roles in T-cell traction forces. *Proc. Natl. Acad. Sci.* *111*, 2241–2246.
- Basu, R. *et al.* (2016). Cytotoxic T Cells Use Mechanical Force to Potentiate Target Cell Killing. *Cell* *165*, 100–110.
- Basu, R., and Huse, M. (2017). Mechanical Communication at the Immunological Synapse. *Trends Cell Biol.* *27*, 241–254.
- Binnig, G., Quate, C. F., and Gerber, C. (1986). Atomic Force Microscope. *Phys. Rev. Lett.* *56*, 930–933.
- Bornschlogl, T., Romero, S., Vestergaard, C. L., Joanny, J.-F., Van Nhieu, G. T., and Bassereau, P. (2013). Filopodial retraction force is generated by cortical actin dynamics and controlled by reversible tethering at the tip. *Proc. Natl. Acad. Sci.* *110*, 18928–18933.
- Bufl, N., Saitakis, M., Dogniaux, S., Buschinger, O., Bohineust, A., Richert, A., Maurin, M., Hivroz, C., and Asnacios, A. (2015). Human Primary Immune Cells Exhibit Distinct Mechanical Properties that Are Modified by Inflammation. *Biophys. J.* *108*, 2181–2190.
- Colbert, M.-J., Raegen, a N., Fradin, C., and Dalnoki-Veress, K. (2009). Adhesion and membrane tension of single vesicles and living cells using a micropipette-based technique. *Eur. Phys. J. E. Soft Matter* *30*, 117–121.
- Comrie, W. A., and Burkhardt, J. K. (2016). Action and traction: Cytoskeletal control of receptor triggering at the immunological synapse. *Front. Immunol.* *7*, 1–25.
- Dembo, M., and Wang, Y. L. (1999). Stresses at the cell-to-substrate interface during locomotion of fibroblasts. *Biophys J* *76*, 2307–2316.
- Depoil, D., and Dustin, M. L. (2014). Force and affinity in ligand discrimination by the TCR. *Trends Immunol.* *35*, 597–603.
- Desprat, N., Guiroy, A., and Asnacios, A. (2006). Microplates-based rheometer for a single living cell. *Rev. Sci. Instrum.* *77*, 55111.
- Dustin, M. L. (2008). Hunter to Gatherer and Back: Immunological Synapses and Kinapses as Variations on the Theme of Amoeboid Locomotion. *Annu. Rev. Cell Dev. Biol.* *24*, 577–596.
- Edelstein, A. D., Tsuchida, M. a, Amodaj, N., Pinkard, H., Vale, R. D., and Stuurman, N. (2014). Advanced methods of microscope control using μ Manager software. *J. Biol. Methods* *1*, 10.
- Étienne, J., Fouchard, J., Mitrossilis, D., Bufl, N., Durand-Smet, P., and Asnacios, A. (2015). Cells as liquid motors: Mechanosensitivity emerges from collective dynamics of actomyosin cortex. *Proc. Natl. Acad. Sci.* *112*, 2740–2745.
- Evans, E., and Kukan, B. (1984). Passive material behavior of granulocytes based on large deformation and recovery after deformation tests. *Blood*, 1028–1035.
- Evans, E., Leung, A., and Zhelev, D. (1993). Synchrony of cell spreading and contraction force as phagocytes engulf large pathogens. *J. Cell Biol.* *122*, 1295–1300.
- Gourier, C., Jegou, A., Husson, J., and Pincet, F. (2008). A Nanospring Named Erythrocyte. The Biomembrane Force Probe. *Cell. Mol. Bioeng.* *1*, 263–275.
- Guillou, L., Babataheri, A., Puech, P.-H., Barakat, A. I., and Husson, J. (2016a). Dynamic monitoring of cell mechanical properties using profile microindentation. *Sci. Rep.* *6*, 21529.
- Guillou, L., Babataheri, A., Saitakis, M., Bohineust, A., Dogniaux, S., Hivroz, C., Barakat, A. I., and Husson, J. (2016b). T lymphocyte passive deformation is controlled by unfolding of

- membrane surface reservoirs. *Mol. Biol. Cell* 27, 3574–3582.
- Heinrich, V., and Ounkomol, C. (2007). Force versus axial deflection of pipette-aspirated closed membranes. *Biophys. J.* 93, 363–372.
- Herant, M., Heinrich, V., and Dembo, M. (2005). Mechanics of neutrophil phagocytosis: behavior of the cortical tension. *J. Cell Sci.* 118, 1789–1797.
- Herant, M., Heinrich, V., and Dembo, M. (2006). Mechanics of neutrophil phagocytosis: experiments and quantitative models. *J. Cell Sci.* 119, 1903–1913.
- Hivroz, C., and Saitakis, M. (2016). Biophysical Aspects of T Lymphocyte Activation at the Immune Synapse. *Front. Immunol.* 7, 1–12.
- Hochmuth, R. M. (2000). Micropipette aspiration of living cells. *J. Biomech.* 33, 15–22.
- Hogan, B., Babataheri, A., Hwang, Y., Barakat, A. I., and Husson, J. (2015). Characterizing Cell Adhesion by Using Micropipette Aspiration. *Biophys. J.* 109, 209–219.
- Howard, J., and Hudspeth, a J. (1987). Mechanical relaxation of the hair bundle mediates adaptation in mechano-electrical transduction by the bullfrog's saccular hair cell. *Proc. Natl. Acad. Sci. U. S. A.* 84, 3064–3068.
- Hu, K. H., and Butte, M. J. (2016). T cell activation requires force generation. *J. Cell Biol.* 213, 535–542.
- Hui, K. L., Balagopalan, L., Samelson, L. E., and Upadhyaya, A. (2015). Cytoskeletal forces during signaling activation in Jurkat T-cells. *Mol. Biol. Cell* 26, 685–695.
- Hui, K. L., and Upadhyaya, A. (2017). Dynamic microtubules regulate cellular contractility during T-cell activation. *Proc. Natl. Acad. Sci.* 114, E4175–E4183.
- Husson, J., Chemin, K., Bohineust, A., Hivroz, C., and Henry, N. (2011). Force Generation upon T Cell Receptor Engagement. *PLoS One* 6, e19680.
- Husson, J., Dogterom, M., and Pincet, F. (2009). Force spectroscopy of a single artificial biomolecule bond: The Kramers' high-barrier limit holds close to the critical force. *J. Chem. Phys.* 130, 2–5.
- Inagaki, N., and Katsuno, H. (2017). Actin Waves: Origin of Cell Polarization and Migration? *Trends Cell Biol.* xx, 1–12.
- Ingber, D. E. (1997). Tensegrity: the Architectural Basis of Cellular Mechanotransduction. *Annu. Rev. Physiol.* 59, 575–599.
- Ishijima, a, Kojima, H., Higuchi, H., Harada, Y., Funatsu, T., and Yanagida, T. (1996). Multiple- and single-molecule analysis of the actomyosin motor by nanometer-piconewton manipulation with a microneedle: unitary steps and forces. *Biophys. J.* 70, 383–400.
- Laan, L., Husson, J., Munteanu, E. L., Kerssemakers, J. W. J., and Dogterom, M. (2008). Force-generation and dynamic instability of microtubule bundles. *Proc. Natl. Acad. Sci. U. S. A.* 105, 8920–8925.
- Lee, C. Y., Thompson, G. R., Hastey, C. J., Hodge, G. C., Lunetta, J. M., Pappagianis, D., and Heinrich, V. (2015). Coccidioides endospores and spherules draw strong chemotactic, adhesive, and phagocytic responses by individual human neutrophils. *PLoS One* 10, 1–28.
- Liu, B., Chen, W., and Zhu, C. (2015). Molecular Force Spectroscopy on Cells. *Annu. Rev. Phys. Chem.* 66, 427–451.
- Liu, Y., Blanchfield, L., Ma, V. P.-Y., Andargachew, R., Galior, K., Liu, Z., Evavold, B., and Salaita, K. (2016). DNA-based nanoparticle tension sensors reveal that T-cell receptors transmit defined pN forces to their antigens for enhanced fidelity. *Proc. Natl. Acad. Sci. U. S. A.*, 201600163.
- Marcy, Y., Prost, J., Carlier, M.-F., and Sykes, C. (2004). Forces generated during actin-based propulsion: a direct measurement by micromanipulation. *Proc. Natl. Acad. Sci. U. S. A.* 101, 5992–5997.
- Marsh, G., and Waugh, R. E. (2013). Quantifying the Mechanical Properties of the Endothelial Glycocalyx with Atomic Force Microscopy. *J. Vis. Exp.*, 1–7.
- Martinelli, R., Zeiger, A. S., Whitfield, M., Sciuto, T. E., Dvorak, A., Van Vliet, K. J., Greenwood, J., and Carman, C. V. (2014). Probing the biomechanical contribution of the endothelium to lymphocyte migration: diapedesis by the path of least resistance. *J. Cell Sci.* 127,

3720–3734.

Merkel, R., Nassoy, P., Leung, A., Ritchie, K., and Evans, E. (1999). Energy landscapes of receptor-ligand bonds explored with dynamic force spectroscopy. *Nature* 397, 50–53.

Meyhöfer, E., and Howard, J. (1995). The force generated by a single kinesin molecule against an elastic load. ... *Natl. Acad. ...* 92, 574.

Mitrossilis, D., Fouchard, J., Pereira, D., Postic, F., Richert, A., Saint-Jean, M., and Asnacios, A. (2010). Real-time single-cell response to stiffness. *Proc. Natl. Acad. Sci. U. S. A.* 107, 16518–16523.

Needham, D., and Hochmuth, R. M. (1992). A sensitive measure of surface stress in the resting neutrophil. *Biophys. J.* 61, 1664–1670.

Niedergang, F., Di Bartolo, V., and Alcover, A. (2016). Comparative Anatomy of Phagocytic and Immunological Synapses. *Front. Immunol.* 7, 1–9.

Ossola, D., Amarouch, M. Y., Behr, P., Vörös, J., Abriel, H., and Zambelli, T. (2015). Force-controlled patch clamp of beating cardiac cells. *Nano Lett.* 15, 1743–1750.

Ounkomol, C., Xie, H., Dayton, P. a, and Heinrich, V. (2009). Versatile horizontal force probe for mechanical tests on pipette-held cells, particles, and membrane capsules. *Biophys. J.* 96, 1218–1231.

Pelling, A. E., Veraitch, F. S., Pui-Kei Chu, C., Nicholls, B. M., Hemsley, A. L., Mason, C., and Horton, M. A. (2007). Mapping correlated membrane pulsations and fluctuations in human cells. *J. Mol. Recognit.* 20, 467–475.

Pincet, F., and Husson, J. (2005). The Solution to the Streptavidin-Biotin Paradox: The Influence of History on the Strength of Single Molecular Bonds. *Biophys. J.* 89, 4374–4381.

Plotnikov, S. V, and Waterman, C. M. (2013). Guiding cell migration by tugging. *Curr. Opin. Cell Biol.* 25, 619–626.

Puech, P.-H. (2005). Measuring cell adhesion forces of primary gastrulating cells from zebrafish using atomic force microscopy. *J. Cell Sci.* 118, 4199–4206.

Rigato, A., Miyagi, A., Scheuring, S., and Rico, F. (2017). High-frequency microrheology reveals cytoskeleton dynamics in living cells. *Nat. Phys.*

Roybal, K. T. *et al.* (2016). Computational spatiotemporal analysis identifies WAVE2 and cofilin as joint regulators of costimulation-mediated T cell actin dynamics. *Sci. Signal.* 9, rs3-rs3.

Saitakis, M., Dogniaux, S., Goudot, C., Bufi, N., Asnacios, S., Maurin, M., Randriamampita, C., Asnacios, A., and Hivroz, C. (2017). Different TCR-induced T lymphocyte responses are potentiated by stiffness with variable sensitivity. *Elife* 6, 1–29.

Sato, M., Levesque, M. J., and Nerem, R. M. (1987). Micropipette aspiration of cultured bovine aortic endothelial cells exposed to shear stress. *Arterioscler. Thromb. Vasc. Biol.* 7, 276–286.

Schaefer, A., and Hordijk, P. L. (2015). Cell-stiffness-induced mechanosignaling - a key driver of leukocyte transendothelial migration. *J. Cell Sci.* 128, 2221–2230.

Schneider, C. a, Rasband, W. S., and Eliceiri, K. W. (2012). NIH Image to ImageJ: 25 years of image analysis. *Nat. Methods* 9, 671–675.

Shao, J. Y., and Hochmuth, R. M. (1996). Micropipette suction for measuring piconewton forces of adhesion and tether formation from neutrophil membranes. *Biophys. J.* 71, 2892–2901.

Sheetz, M. P. (1994). Cell migration by graded attachment to substrate and contraction. *Semin Cell Biol.* 5, 149–155.

Simson, D. a, Ziemann, F., Strigl, M., and Merkel, R. (1998). Micropipet-based pico force transducer: in depth analysis and experimental verification. *Biophys. J.* 74, 2080–2088.

Sit, P., Spector, A., Lue, A., Popel, A., and Brownell, W. (1997). Micropipette aspiration on the outer hair cell lateral wall. *Biophys. J.* 72, 2812–2819.

Šmít, D., Fouquet, C., Doulazmi, M., Pincet, F., Trembleau, A., and Zapotocky, M. (2017). BFPTool: a software tool for analysis of Biomembrane Force Probe experiments. *BMC Biophys.* 10, 2.

Spillmann, C. M., Lomakina, E., and Waugh, R. E. (2004). Neutrophil adhesive contact dependence on impingement force. *Biophys. J.* 87, 4237–4245.

- Sun, L., Cheng, Q.-H., Gao, H., and Zhang, Y.-W. (2011). A nonlinear characteristic regime of biomembrane force probe. *J. Biomech.* *44*, 662–668.
- Tees, D. F., Waugh, R. E., and Hammer, D. a (2001). A microcantilever device to assess the effect of force on the lifetime of selectin-carbohydrate bonds. *Biophys. J.* *80*, 668–682.
- Tsukasaki, Y., Kitamura, K., Shimizu, K., Iwane, A. H., Takai, Y., and Yanagida, T. (2007). Role of multiple bonds between the single cell adhesion molecules, nectin and cadherin, revealed by high sensitive force measurements. *J. Mol. Biol.* *367*, 996–1006.
- Varma, R., Campi, G., Yokosuka, T., Saito, T., and Dustin, M. L. (2006). T cell receptor-proximal signals are sustained in peripheral microclusters and terminated in the central supramolecular activation cluster. *Immunity* *25*, 117–127.
- Wang, X., and Ha, T. (2013). Defining Single Molecular Forces Required to Activate Integrin and Notch Signaling. *Science (80-.)*. *340*, 991–994.
- Wülfing, C. (1998). A Receptor/Cytoskeletal Movement Triggered by Costimulation During T Cell Activation. *Science (80-.)*. *282*, 2266–2269.

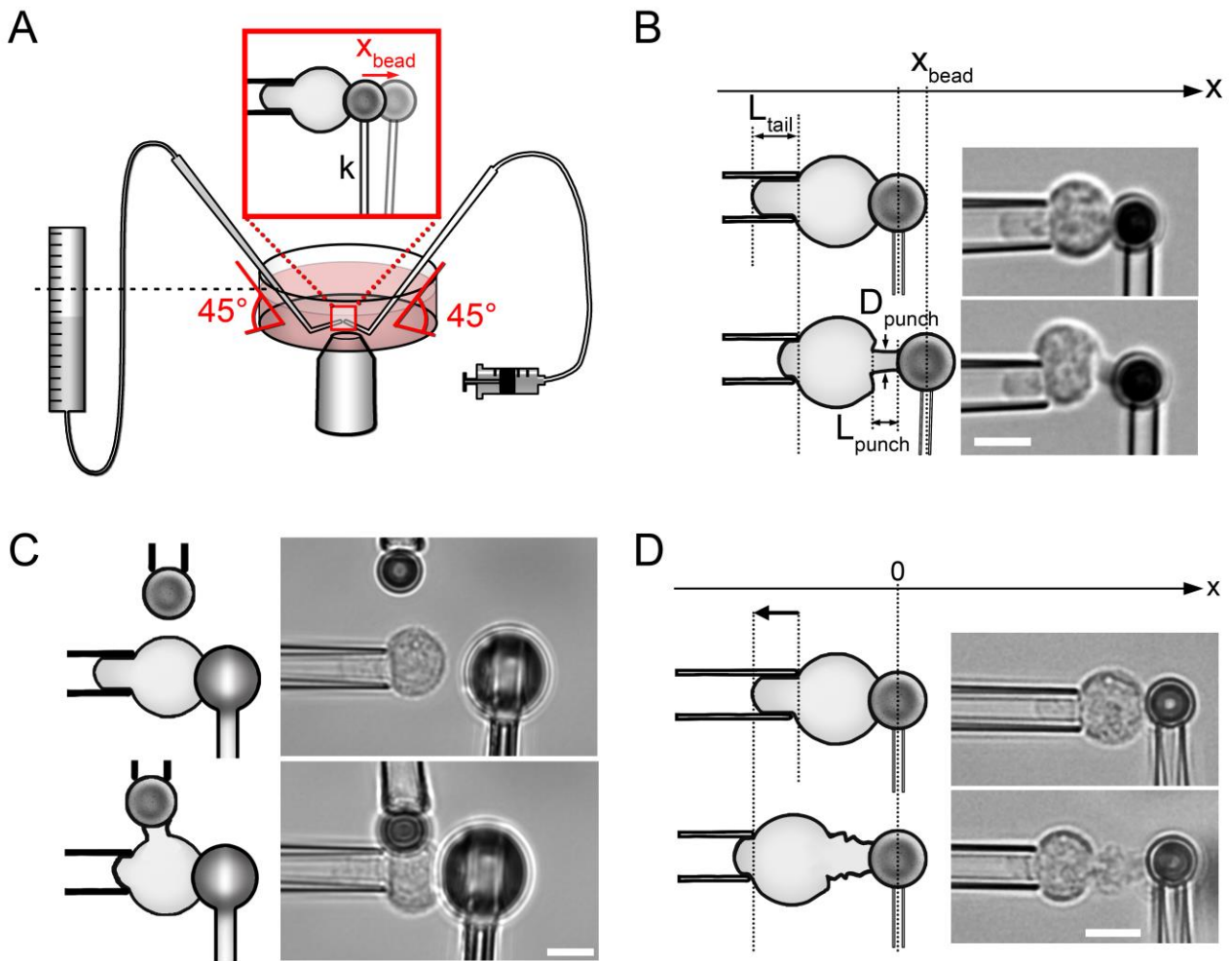


Figure 1. Micropipette setups used in the experiments. (A) Micropipette Force Probe - overview. The tip of a flexible micropipette holding an activating bead (bead micropipette) is positioned close to the tip of a stiff micropipette holding a cell (cell micropipette). Both micropipettes have a 45° -bend so that their tips are in the focal plane of the inverted microscope. During the experiment, the bending of the bead micropipette shows as the displacement of the bead along the x -axis (x_{bead} , see B). The aspiration pressure in the cell micropipette is controlled by the height of a water reservoir. The aspiration pressure in the bead micropipette is controlled with a syringe filled with air. (B) Micropipette Force Probe - geometrical measurements. Drawings of an activating T cell (left) with corresponding brightfield microscopy images (right). Top: the cell is brought in contact with the bead at time $t=0$. Bottom: the cell pushes the bead away during activation. The position x_{bead} of the center of the bead along the x -axis is tracked over time, leading to speed and force measurement. The dimensions of the pushing protrusion called a punch (length L_{punch} and diameter D_{punch}), and the part of the cell inside the micropipette called a tail (length L_{tail}) are measured manually only at the selected frames of the recording. (C) Profile microindentation of a cell during its activation. Drawings (left) and corresponding brightfield images (right). A microindenter replaces the bead micropipette; the bead is held by a third, stiff micropipette. During the experiment the cell is indented once every 10 s, each indentation providing a measurement of the Young's modulus, describing the effective stiffness of the cell. After measuring the Young's modulus baseline value for several cycles (top), the bead is brought in contact with the cell; the indentations continue during the activation (bottom, see Figure 2D). (D) Activation of a cell with no resisting bead micropipette. Drawings (left) and corresponding brightfield images (right). A cell is brought in contact with a bead, and when the punch starts growing from the cell, the cell micropipette is retracted to keep the bead micropipette at its initial position, simulating the cell pushing against a bead micropipette of zero bending stiffness. B-D: scale bar is $5 \mu\text{m}$.

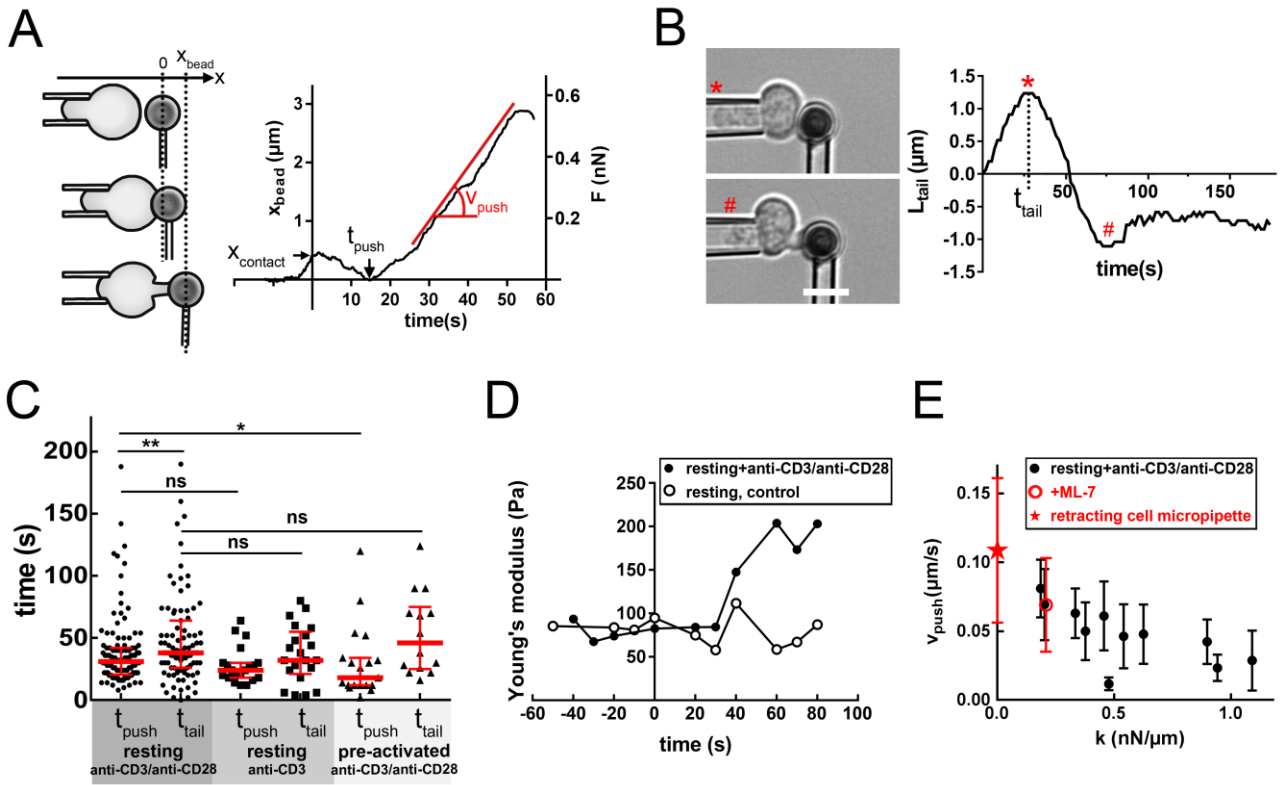


Figure 2. First events during T cell activation. (A) Onset of pushing force. Drawings of a T cell during the beginning of the activation process (left) with the corresponding position of the bead x_{bead} (right). At the beginning of the experiment the bead was located at $x_{bead}=0$ (top drawing); at time $t=0$ contact was made between the cell and the bead (middle drawing), leading to a small displacement of the bead ($x_{contact}$). The cell then reorganized and started growing a protrusion (called a punch, bottom drawing) at time t_{push} and with a speed v_{push} . (B) Measurement of tail length. Brightfield images of a T cell during activation (left), with the corresponding length of the part of the cell that is aspirated in the cell micropipette, L_{tail} (see Figure 1B). At time $t=t_{tail}$, the tail started retracting inside the cell micropipette (red star). In this example the retraction lasted ~ 40 s and stopped at $t\sim 70$ s (red #). Scale bar is $5 \mu\text{m}$. (C) Comparison of timings. Two time points, t_{push} and t_{tail} were measured from contact to the onset of mechanical changes (see A and B), and for activation of human primary $CD4^+$ T cells (resting) with anti-CD3/anti-CD28 beads, or only anti-CD3 beads, and for human $CD4^+$ T lymphoblasts (pre-activated) with anti-CD3/anti-CD28 beads. Each data point represents one cell, red thick line shows median, whiskers span the interquartile range. * $p=0.02$, ** $p=0.04$, two-tailed Mann-Whitney test. (D) Increase in the Young's modulus of a T cell (in its effective stiffness). Full circles: example showing the Young's modulus of a resting T cell during its activation measured with profile microindentations (see Figure 1C). Open circles: a control resting T cell indented with no activating bead. (E) Pushing speed v_{push} depends on the bending stiffness of the bead micropipette k . Full circles: MFP experiments with various bending stiffness of the bead micropipette. Red star: experiment where the cell micropipette was retracted during punch growth in order to simulate zero bending stiffness (see Figure 1D). Open circle: resting T cells treated with $30 \mu\text{M}$ ML-7 (inhibitor of Myosin Light Chain Kinase). Each data point shows mean \pm s.d. over one experimental day (the same bead micropipette), representing 4 to 13 cells ($N=9\pm 3$ cells, mean \pm s.d.).

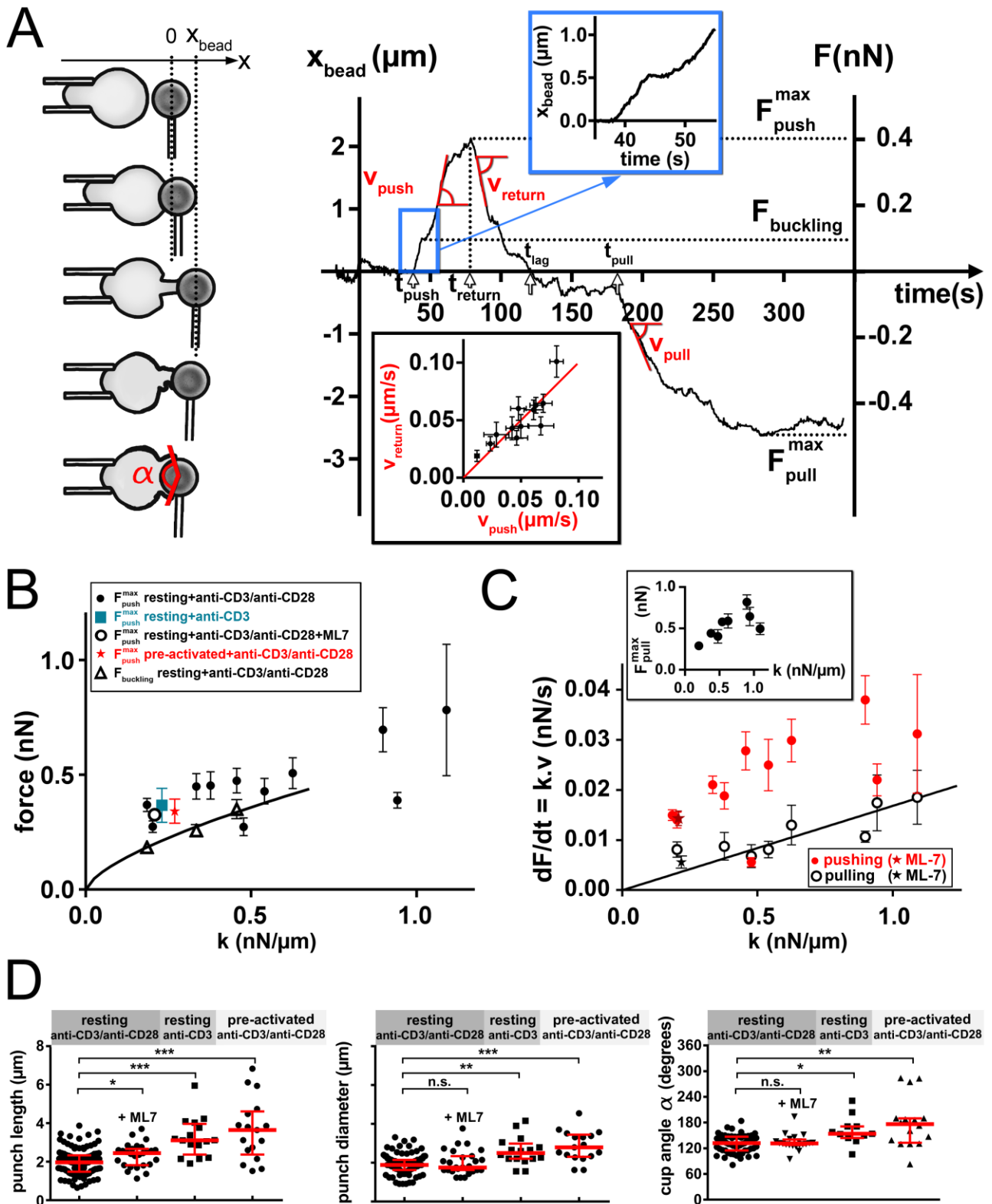


Figure 3. Sequence of mechanical early events during T cell activation. (A) Drawings of a T cell (left) and time trace of the bead position, x_{bead} , and force, F , in the first minutes of T cell activation (right). Inset at bottom: return speed v_{return} vs pushing speed v_{push} . The line is a linear regression, with a slope of 1.0. Inset on top: magnification of the stalling of the bead when the punch buckled. (B) Maximal pushing force and buckling force. The continuous line corresponds to the buckling force of an elastic beam (see text). Each data point shows mean \pm s.e.m. over one experimental day, representing 5 to 14 cells ($N=9 \pm 3$, mean \pm s.d.). (C) Loading rate dF/dt (force in absolute value) during pushing (full circles) or pulling (open circles) vs bending stiffness of the bead micropipette k .

*The line corresponds to a linear fit of the pulling loading rate (see text). Each data point shows mean±s.e.m. over one experimental day, representing 3 to 10 cells (N=7±2, mean±s.d.). Inset: maximal pulling force, F_{pull}^{max} , vs bending stiffness of the bead micropipette k . (D) Dimensions of the pushing protrusion (punch, left and middle) and the pulling protrusion (cup, right). The punch length and diameter were measured when the punch was the longest (see Figure 1B), the cup coverage angle on the bead, α , was measured as soon as the cup was formed (see the bottom drawing in A) * $p < 0.05$, ** $p < 0.01$, *** $p < 0.001$ two-tailed unpaired t-test with Welch's correction.*

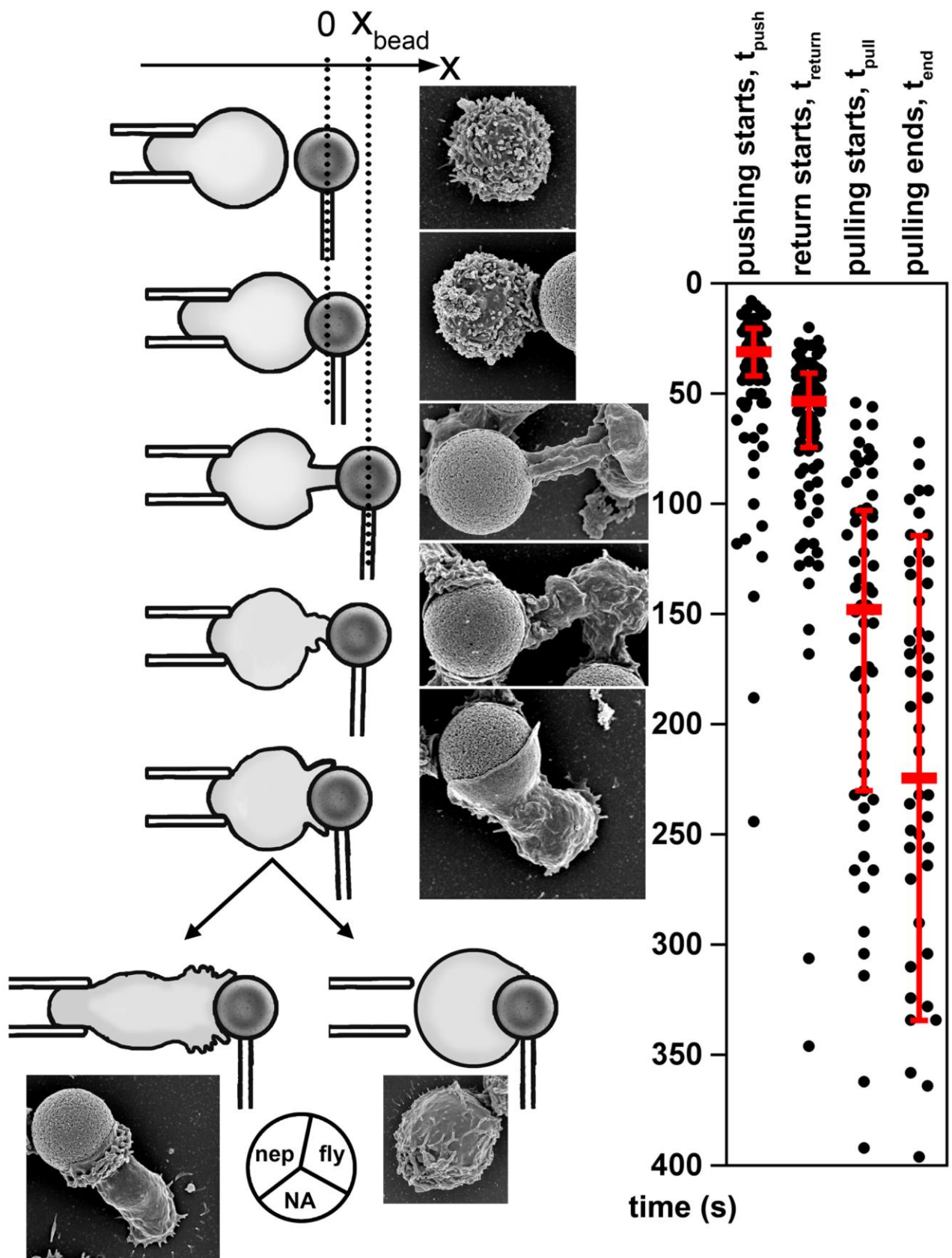


Figure 4. Morphology of T cells during early stages of activation. Drawings of T cells (left) with corresponding examples of cells imaged with scanning electron microscopy (SEM, right). The SEM images were cropped from larger fields of view, see Supplemental Figure S3B. Beads are 4.5 μm in diameter. The pie chart shows the proportion of the two morphological types in the population, nep

– nepenthes, fly – flytrap, NA – not assigned (N=77 resting T cells activated with anti-CD3/anti-CD28 beads in 8 experiments). Timeline shows the different phases of the activation process (see chart in the Figure 3A), for resting T cells activated with anti-CD3/anti-CD28 beads. Each dot is a single cell, red thick line shows the median, whiskers span the IQR.

Supplemental Materials

Molecular Biology of the Cell

Sawicka et al.

SUPPLEMENTAL MATERIAL

Micropipette Force Probe to quantify single-cell force generation: application to T cell activation.

Anna Sawicka^{†,‡}, Avin Babataheri[†], Stéphanie Dogniaux[‡], Abdul I. Barakat[†], David Gonzalez-Rodriguez[§], Claire Hivroz^{*,*}, Julien Husson^{†,*}

*For correspondence: claire.hivroz@curie.fr (CH), julien.husson@ladhyx.polytechnique.fr (JH)

[†]Laboratoire d'Hydrodynamique (LadHyX), Department of Mechanics, Ecole polytechnique-CNRS UMR7646, 91128 Palaiseau, France.

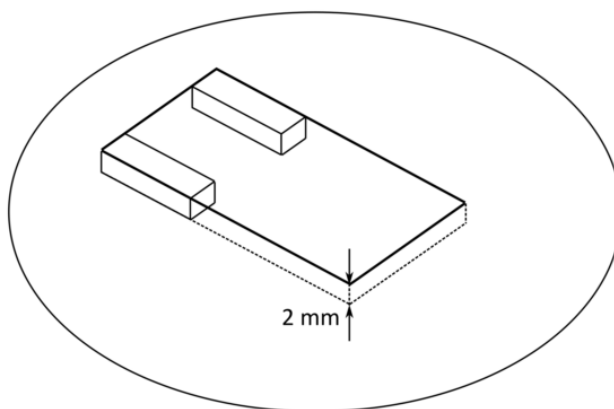
[‡]Institut Curie Section Recherche, INSERM U932 & PSL Research University, Paris, France.

[§]LCP-A2MC, Institut Jean Barriol, Université de Lorraine, 1 bd Arago, 57078 Metz, France.

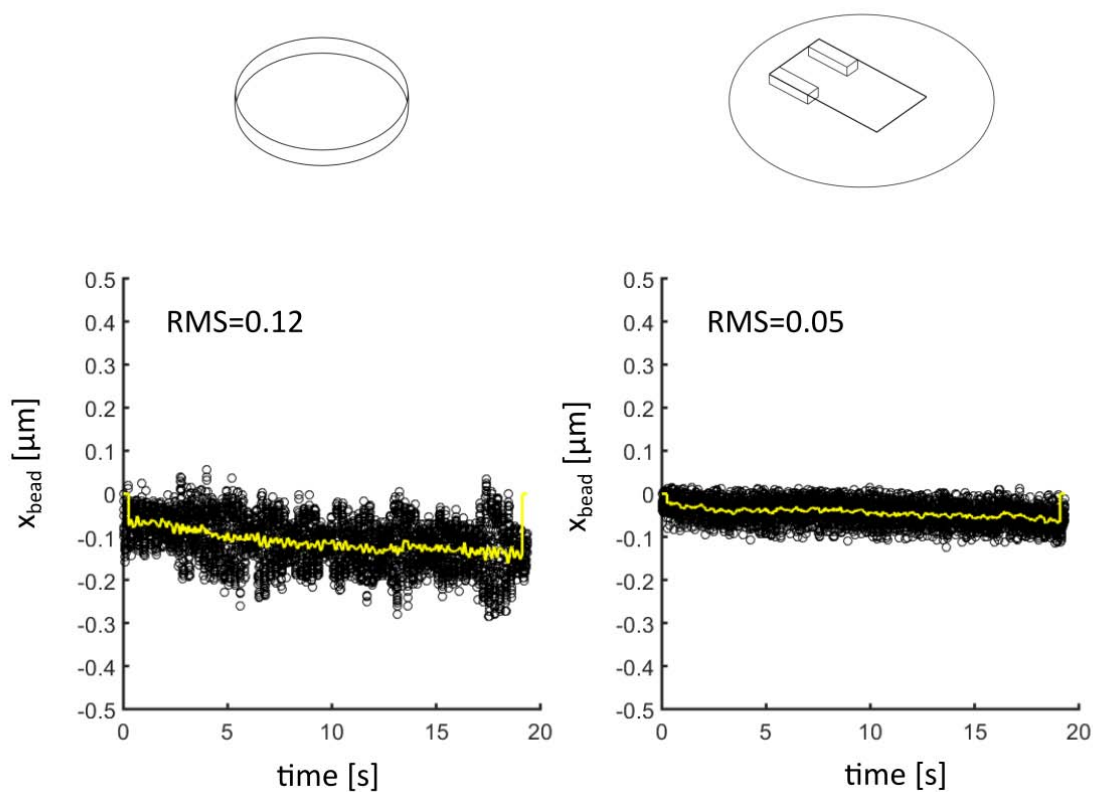
This file contains Supplemental Figures S1-S9 (pages 2-10) and the description of Videos 1-6 (page 11).

SUPPLEMENTAL FIGURES

A

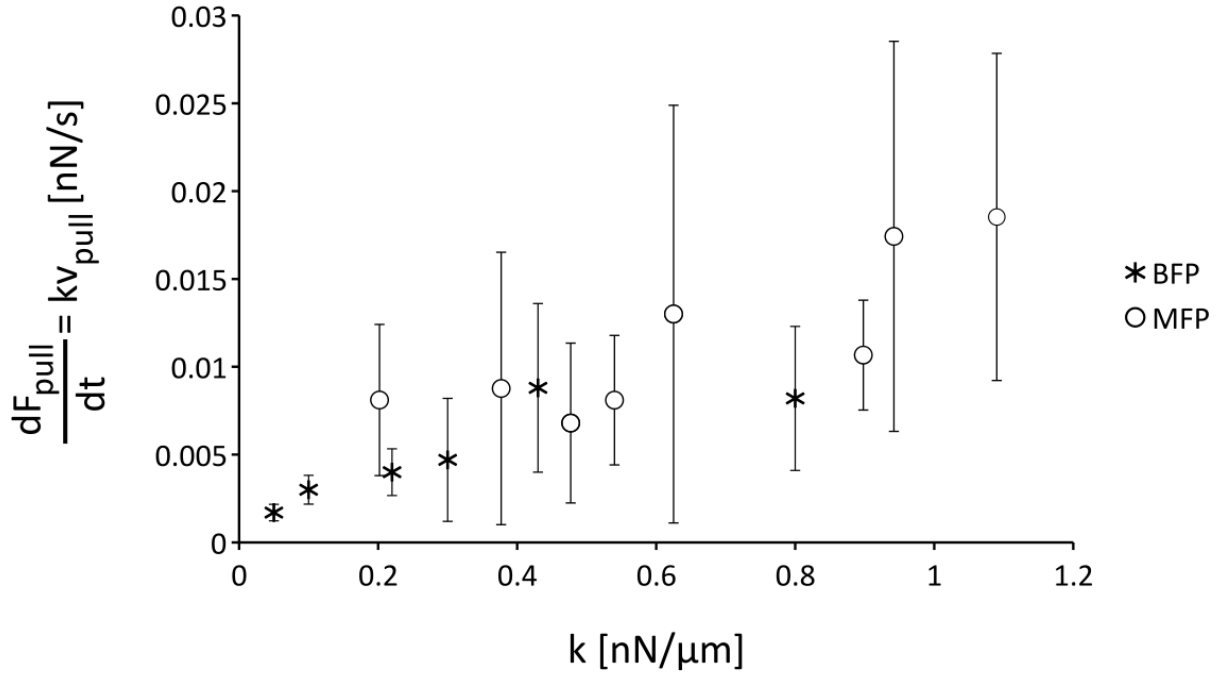


B

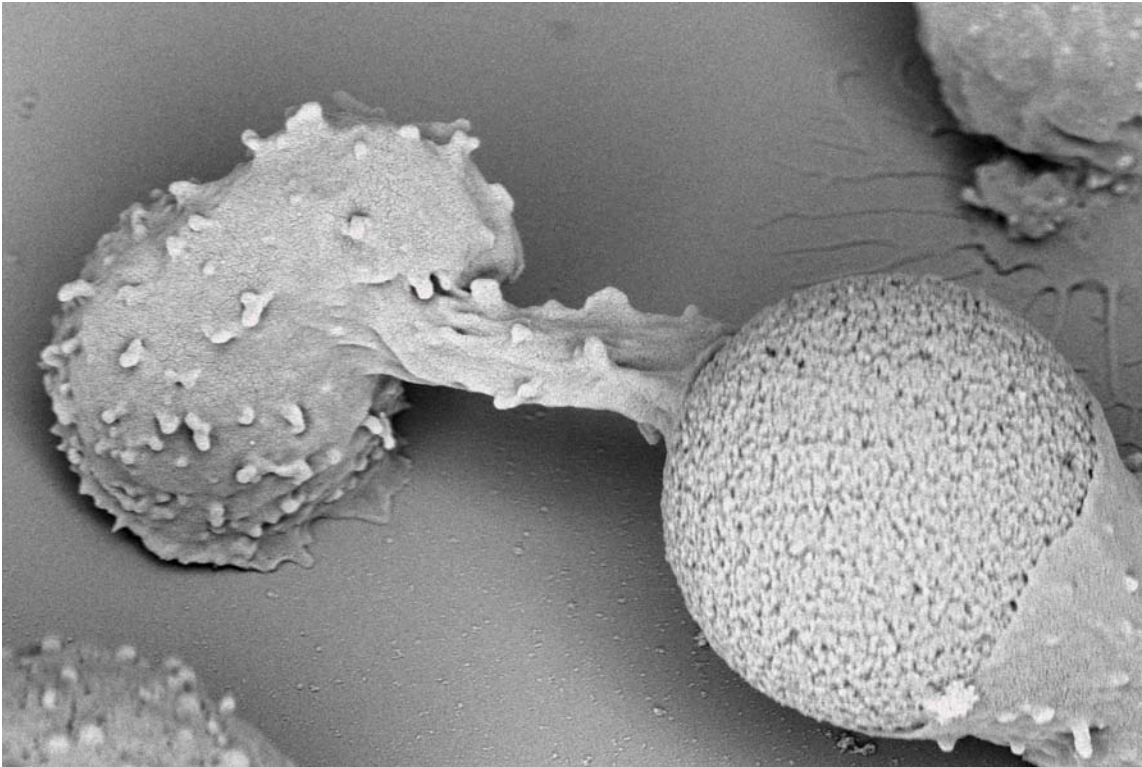


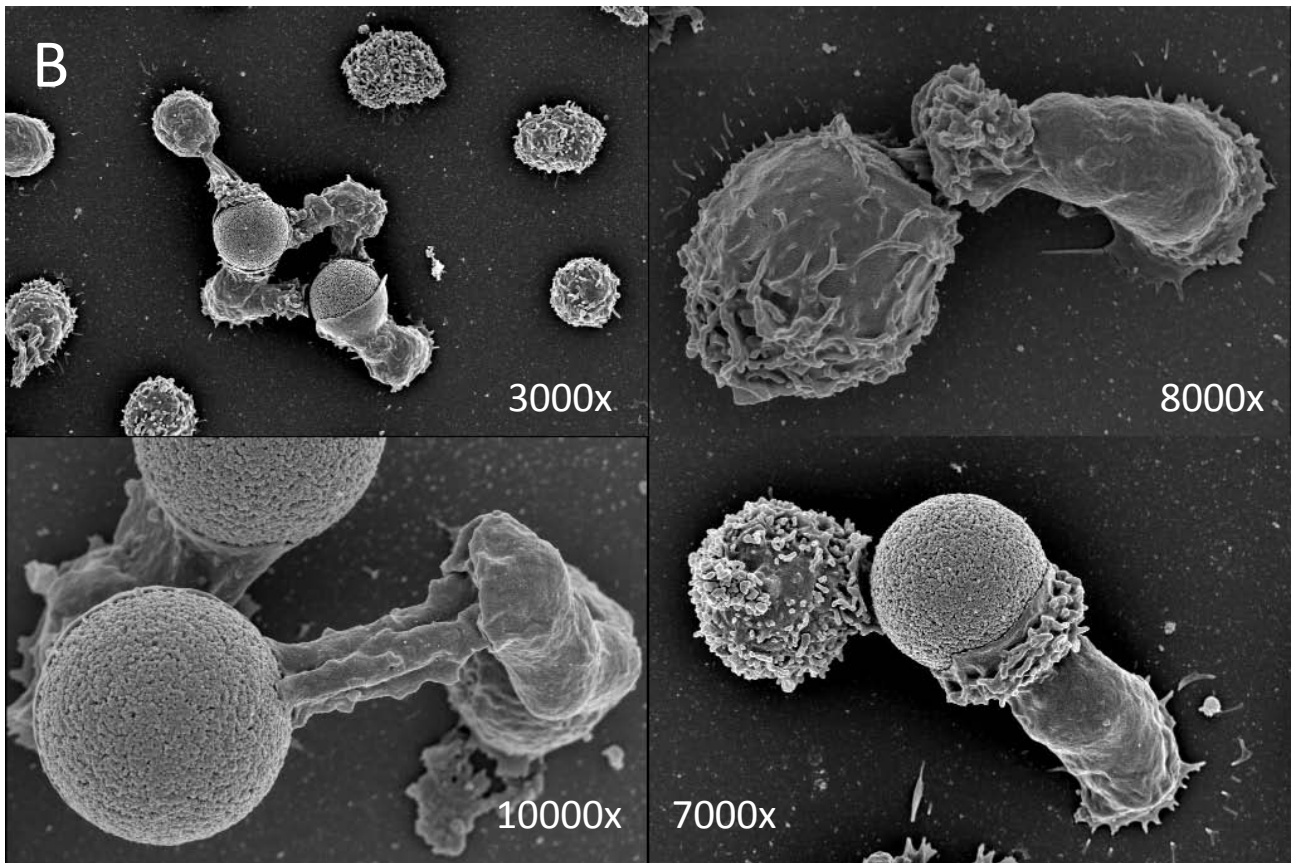
SUPPLEMENTAL FIGURE S1. Experimental chamber with a glass roof reduces the bead micropipette vibrations. (A) Design of the chamber made of two glass coverslips (50 mm diameter at the bottom, 8x24 mm on top, Thermo Scientific Menzel) spaced with two pieces of adhesive paste (patafix, UHU France, Courbevoie, France). The space between the two cover slips is filled with medium; micropipettes are inserted through the open part at the front. (B) Timetrace of the position of the tip of a bead micropipette of bending stiffness $k=0.51$ nN/ μm , placed in an open Petri dish filled with medium (left) and in the experimental chamber (right). Individual data points acquired at a frequency of 400 Hz are shown in black, a window average over 50 data points is

shown as a yellow line. Vibrations were measured at room temperature. Root mean square value (RMS) is reported for both datasets.

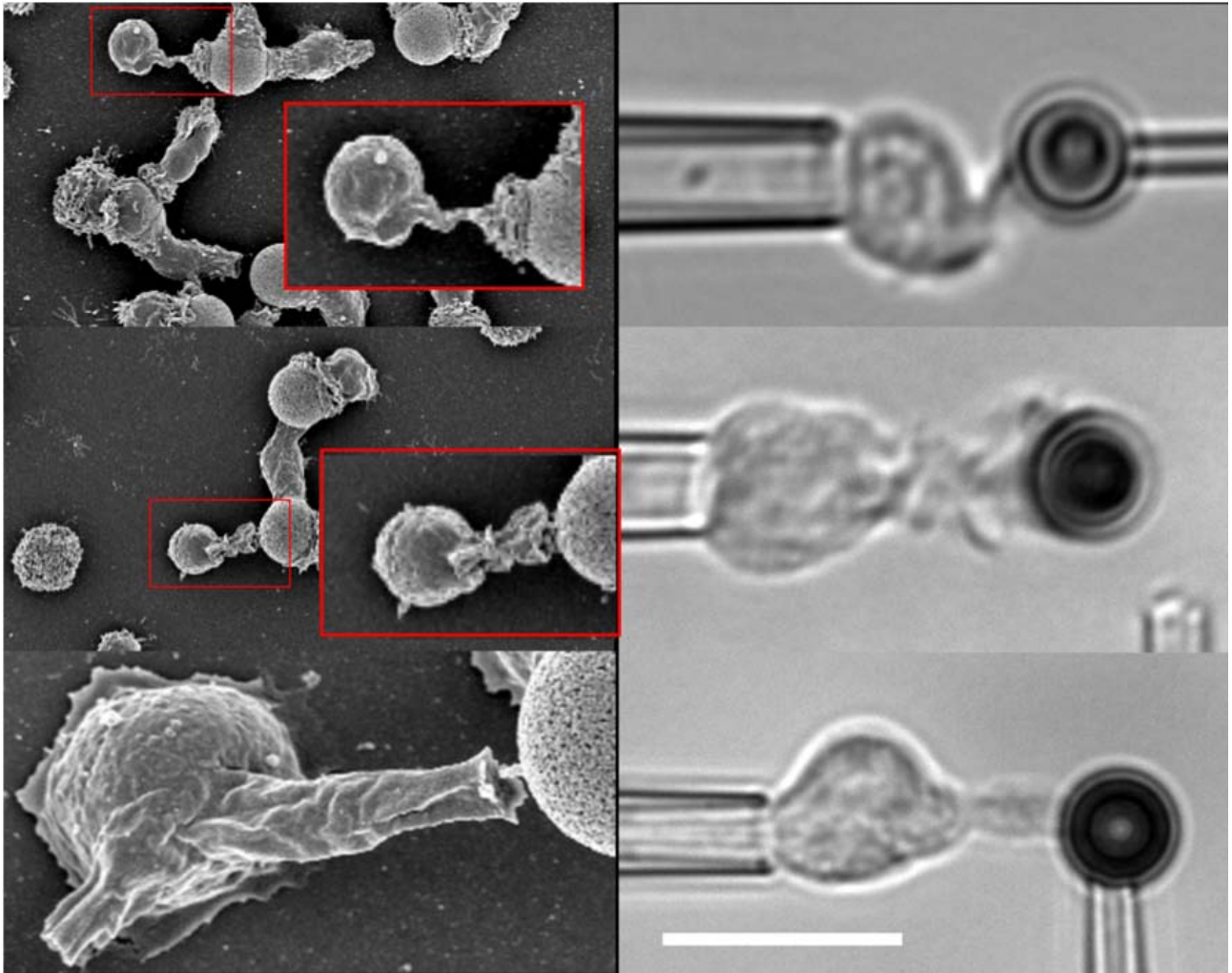


SUPPLEMENTAL FIGURE S2. Comparison between the Micropipette Force Probe (MFP) and the Biomembrane Force Probe (BFP). The pulling loading rate was measured for the activation of human primary CD4+ T cells with anti-CD3/anti-CD28 beads (MFP) and anti-CD3 beads (BFP). The BFP data was published before (Husson, J., Chemin, K., Bohineust, A., Hivroz, C., and Henry, N. (2011). Force Generation upon T Cell Receptor Engagement. PLoS One 6, e19680.), the MFP data are in Figure 3C. Each data point shows mean \pm s.d. over one day of experiments, representing 3 to 10 cells (N=7 \pm 2, mean \pm s.d.).

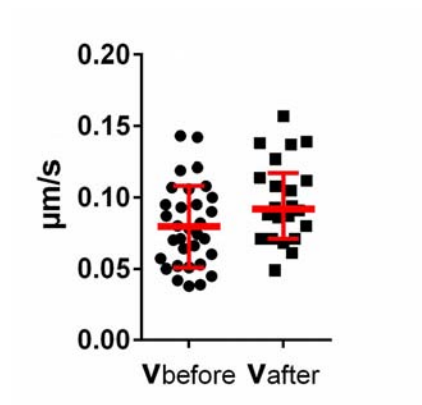




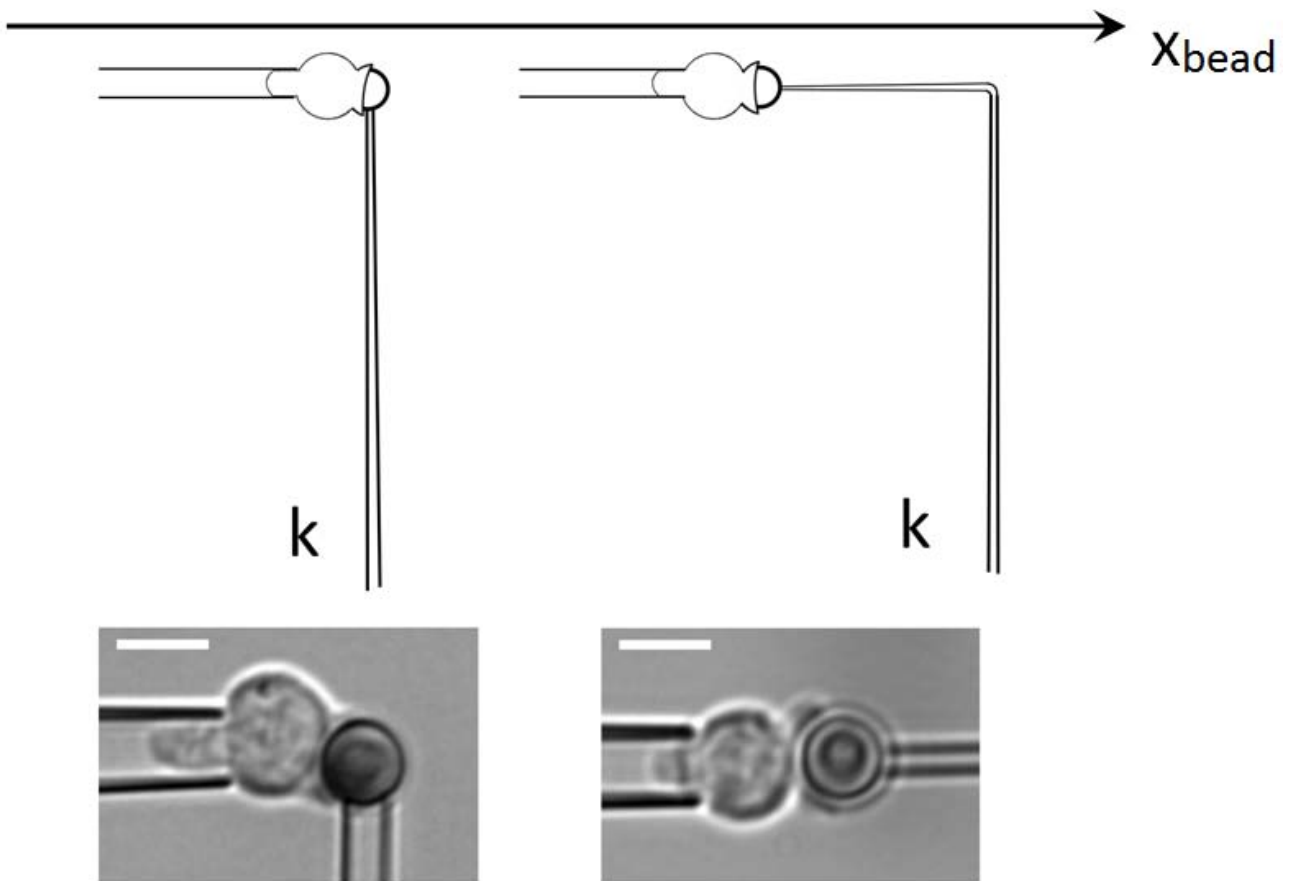
SUPPLEMENTAL FIGURE S3. Scanning Electron Microscopy images of T cell activation. Human primary CD4⁺ T cells were incubated on glass slides coated with poly-L-lysine for 20 minutes. Then, anti-CD3/anti-CD28 beads were added, and cells were fixed 5 minutes later. (A) Pushing protrusion (punch) grows at a sharp angle from the cell body. This image was taken with the sample table tilted at 45° angle. (B) Images used for the insets in Figure 4. Frames with dashed line show the parts that were cropped. The magnification used is marked in each image; beads have the diameter of 4.5 μm.



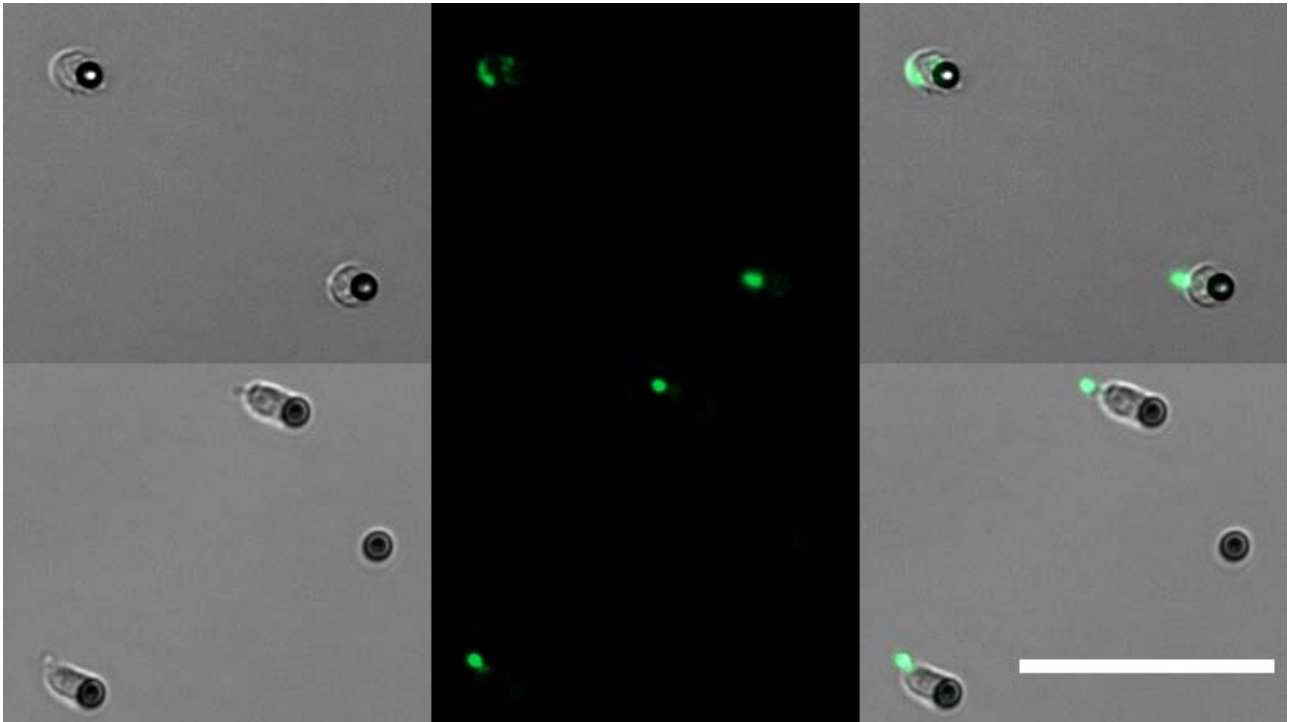
SUPPLEMENTAL FIGURE S4. Examples of the punch morphology during buckling. Scanning Electron Microscopy images (left) and brightfield images chosen based on similarity (right, scale bar is 10 μm). In both cases the T cells were activated with anti-CD3/anti-CD28 beads (4.5 μm diameter). The SEM images were cropped from large views (1000x magnification, insets zoomed 2x, top and middle, and 7000x magnification, bottom image) and show human primary CD4⁺ T cells. The brightfield images show a human primary CD4⁺ T cell (top), a human pre-activated CD4⁺ T cell (T lymphoblast) that picked the bead out of the bead micropipette (middle), and a human primary CD4⁺ T cell during the experiment with the cell micropipette retracted (bottom, see Fig. 1D). Brightfield images show both designs of the bead micropipette (see Supplemental Figure S6).



SUPPLEMENTAL FIGURE S5. Pushing speed after the buckling of the punch is the same as before the buckling. Pushing speed measured before and after buckling (see Figure 3A) for resting human primary CD4⁺ T cells activated with anti-CD3/anti-CD28 beads (N=34). Red thick line shows median, whiskers span the interquartile range.

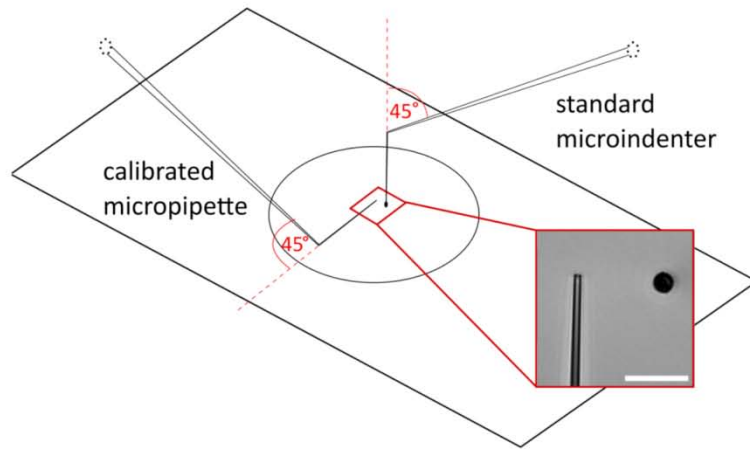


SUPPLEMENTAL FIGURE S6. Two designs for the bead micropipette. Drawings of cell and bead micropipette during an experiment (top) with corresponding brightfield images (bottom). Scale bar is 5 μm in both images. The part of the micropipettes that is vertical in the drawing bends when a cell exerts forces, leading in both cases to the bead movement along the x axis.

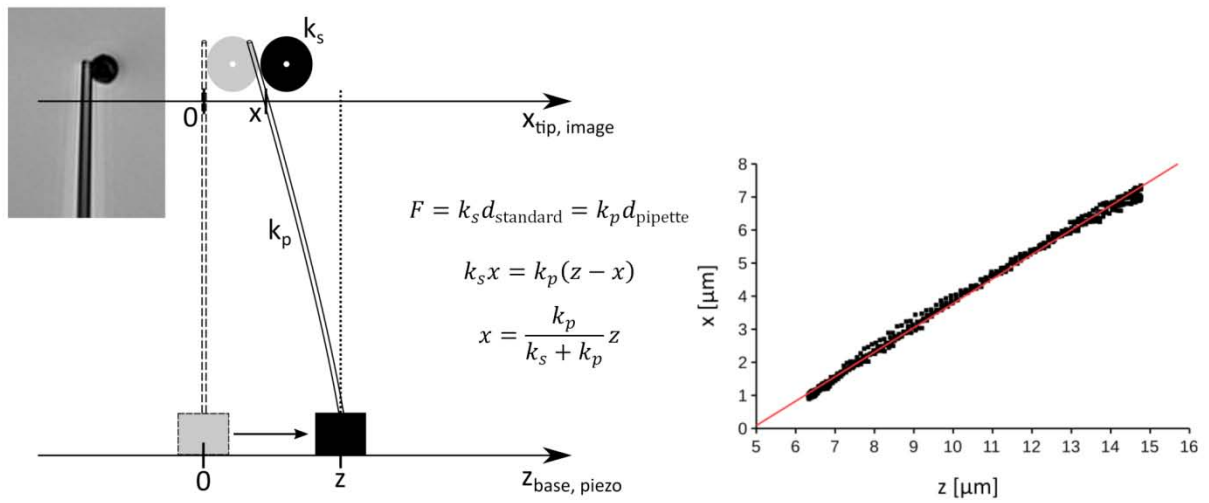


SUPPLEMENTAL FIGURE S7. SiR-actin staining of activated T cells. Human primary CD4⁺ T cells were incubated with 1 μ M SiR-actin and 10 μ M verapamil for 1 h at 37°C, then spinned down (300g, 3 min, room temperature) and imaged in a Petri dish with complete medium and beads. The figure shows two different fields of view during the same experiment. Brightfield images (left), actin filaments in green (middle) and overlay (right). During the activation, the SiR-actin staining moves gradually towards the back of the cell (the side opposite to the bead), and in the end stains the crescent-shape back of the flytrap cells (the cell in the top left corner) and the uropods of the nepenthes cells. See also Video 6. Scale bar is 50 μ m.

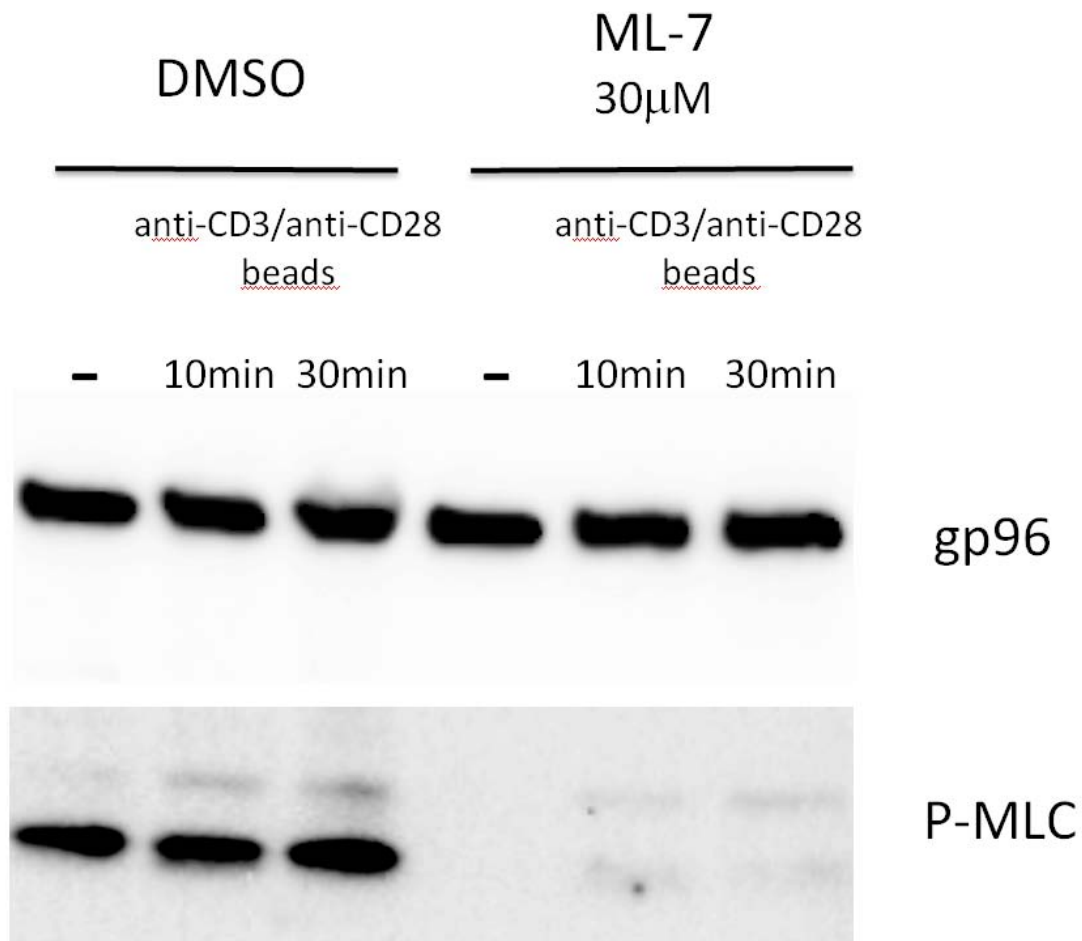
A



B



SUPPLEMENTAL FIGURE S8. Calibration of the bead micropipette. (A) Drawing of the calibration setup. The bead micropipette is placed on the micropositioner with a piezoelectric controller along with a strain gauge reader (Thorlabs, Newton, NJ, USA), which enables the controlled movement of the base of the micropipette. The standard microindenter, of known stiffness, k_s , is held by a second micropositioner, with the tip placed in the microscope field of view. Inset: brightfield image of a micropipette and a microindenter before calibration, scale bar is 20 μm . (B) Calculation of the bending stiffness of the micropipette, k_p . During calibration the micropipette is first brought in contact with the tip of the indenter (brightfield image on the left). Then the base of the micropipette is moved by a distance z , set on the piezoelectric controller. The tip of the micropipette moves together with the tip of the indenter by a smaller distance x , tracked in the microscopy image. The same force causes the bending of the indenter by a distance $d_{\text{standard}} = x$ and the bending of the micropipette by a distance $d_{\text{pipette}} = z - x$. We obtain k_p from the slope of the linear regression of the $x(z)$ plot (right).



SUPPLEMENTAL FIGURE S9. ML-7 treatment of cells inhibits phosphorylation of the myosin light chain (MLC). Human primary CD4⁺ T cells were pre-incubated for 15 minutes at 37°C with 30 μ M ML-7, the MLCK inhibitor, or the vehicle (DMSO) alone. Cells were then activated for 10 to 30 minutes with anti-CD3/anti-CD28 beads in the presence of ML-7. Phosphorylation of the MLC was measured by Western blot analysis. The gp96 protein in each lane is shown as a loading control. Compared to control (DMSO), the cells incubated with ML-7 show less phosphorylation of MLC demonstrating that ML-7 is inhibiting MLCK in our conditions.